A Riemann Ghost Fluid Method for the Godunov-Peshkov-Romenski Model of Continuum Mechanics

Haran Jackson[a,**], Nikos Nikiforakis[a]

[a]*Cavendish Laboratory, JJ Thomson Ave, Cambridge, UK, CB3 0HE*

Abstract

The Godunov-Peshkov-Romenski model of continuum mechanics is claimed to be capable of describing both solids and fluids (both viscous and inviscid) in the same framework [29, 10]. Different solids and fluids are governed by the same set of partial differential equations, differing only in their equations of states and strain dissipation functions. This has the potential to streamline development of simulation software for scenarios involving multiple materials and phases of matter, by reducing the number of different systems of equations that require solvers, and cutting down on the amount of theoretical work required.

At present, there is no way of dealing with material interfaces in the GPR model, however. In this study, a modification of Barton's [3] application of Sambasivan and Udaykumar's Riemann Ghost Fluid Method [36, 37] is devised for the GPR model, enabling the simulation of material interfaces. This new method is tested on a variety of interface problems. It is demonstrated to accurately reproduce analytical results for known Riemann problems, and to produce expected results with regards to heat conduction across interfaces.

Keywords: Godunov-Peshkov-Romenski, GPR, Ghost Fluid Method, RGFM, multimaterial

1. Background

1.1. Multimaterial and Multiphase Models

The definition of a multiphase system is slightly ambiguous in the literature. Here it will be taken to mean a system consisting of either two or more different materials (possibly in the same phase of matter), or two or more volumes of (possibly the same) material in different phases of matter. There are two aspects of multiphase systems that require attention: multiphase flow, and multiphase heat transfer. The latter becomes important when the phases are at different temperatures. In this study, the different phases will be assumed to be immiscible.

Without a unified model of continuum mechanics, capable of describing all phases in the same framework, different sets of equations may have to be used in the different regions occupied by different phases. These systems arise, for example, in fluid-structure interaction, or oil-water interfaces. An overview of current approaches to multiphase systems will now be given. The examples here are illustrative but not exhaustive.

There has been a huge amount of research activity in the field over the years, but current approaches can be broadly classified as either monolithic or partitioned [19]. In a monolithic scheme, all phases are described by the same set of nonlinear equations.

The evolution of the interfaces is implicit to the equations, unlike in partitioned schemes. See for example [26, 20]. The system is solved by a multivariate Newton-type method. It is often ill-conditioned, due to the different scales of the state variables of the different phases. Thus, iterative solvers are required, proving inefficient unless good preconditioners are available. Codes tend to be very specialized to the specific problems they solve, and it requires expertise to develop and maintain such methods.

In a partitioned scheme, the states of the different phases are calculated separately at each time step, possibly using different models. See Rossi and Oñate [34] for a recent overview of some of the common algorithmic features of these schemes. The individual systems do not suffer from the scaling-induced conditioning problems of monolithic schemes, but attention now needs to be payed to the material interfaces. Modeling them can be unstable and relatively computationally expensive (although typically not as expensive as solving the full monolithic systems). One of the great benefits of partitioned schemes is that legacy implementations of common models may be used in the domains occupied by materials that they describe. These implementations are often well-used and relatively bug free, and tend to be written efficiently for the kinds of problems that the solve. As an example of a software suite taking advantage of this, see the Caltech's Virtual Test Facility [1].

Under both types of schemes, the models describing the different phases may be formulated in either a Lagrangian, an Eulerian, or an ALE framework. Solids models tend to come in Lagrangian form, and often these are combined with ALE

---
[*]Corresponding author
[**]Principal corresponding author
Email address: `hj305@cam.ac.uk` (Haran Jackson)

forms for the fluid phases, so that the fluid meshes may deform to match the deformation of the solid (see, for example, Pin et al. [30]). These schemes tend to be very accurate, but like all Lagrangian schemes, they fail if the meshes become highly contorted. Thus, adaptive remeshing is often necessary. Some authors have coupled a Lagrangian solid scheme with an Eulerian fluid scheme, but extra care must be taken when applying the boundary conditions to the interface, which corresponds to the intersection of the Eulerian and Lagrangian meshes (see Legay et al. [21] for an implementation using level sets, or Fedkiw [12] for a GFM coupling). Some authors, such as Ryzhakov et al. [35], have found success in using the common Lagrangian formulations for the solid, and a reformulated Lagrangian model for the fluid, implementing the necessary adaptive remeshing. Yet another option is to model both the fluid and the solid in an Eulerian framework, although this now necessitates a level set method or volume of fluid method [18] to track the interfaces. Also, these methods are more prone to losing small-scale geometric features of the media, unless methods such as AMR are employed to combat this [19].

In a recently submitted paper, Michael and Nikiforakis [25] (building on the work of Schoch et al. [38]) couple various Eulerian models of reactive and inert fluids and solids by use of a Riemann Ghost Fluid Method, with the ghost states calculated using specialised mixed-material Riemann solvers for each interaction (see Section 1.3). Whilst these techniques do not suffer from the mesh contortion issues inherent in Lagrangian formulations of continuum mechanics, and the interface coupling tends to be less computationally expensive than the iterative techniques demanded by monolithic schemes, a fair amount of theoretical work needs to be done to derive analytical relations describing the interactions between every pair of models used.

If it were possible to describe all phases with the same Eulerian model, this method could be used, with only one type of Riemann solver needed to cope with any multiphase problem posed. This would effectively be a partitioned scheme with the same system solved in each domain. The GPR model represents such an opportunity. As will be seen, the model also includes terms for heat conduction, which do not appear in the basic formulations of many of the common models used in multiphase systems (e.g. the Euler equations, or the Navier-Stokes equations). Heat conduction is often ignored in multiphase modeling, but such a framework based on the GPR model would almost unavoidably include it. It should be noted, though, that any unified model of continuum mechanics purporting to describe all phases of interest must be at least as descriptive as competing models tailored to each individual phase if the utmost model fidelity is required. Although the results for the GPR model applied to standard test cases have been promising, both here and in other preliminary studies [10, 6], more work is required to determine how faithfully the GPR model reproduces common agreed phenomenological results.

1.2. The Model of Godunov, Peshkov and Romenski

The GPR model, first introduced by Peshkov and Romenski [29] and expanded upon by Dumbser et al. [10], takes the following form:

$$\frac{\partial \rho}{\partial t} + \frac{\partial (\rho v_k)}{\partial x_k} = 0 \tag{1a}$$

$$\frac{\partial (\rho v_i)}{\partial t} + \frac{\partial (\rho v_i v_k + p\delta_{ik} - \sigma_{ik})}{\partial x_k} = 0 \tag{1b}$$

$$\frac{\partial A_{ij}}{\partial t} + \frac{\partial (A_{ik} v_k)}{\partial x_j} + v_k \left(\frac{\partial A_{ij}}{\partial x_k} - \frac{\partial A_{ik}}{\partial x_j} \right) = -\frac{\psi_{ij}}{\theta_1(\tau_1)} \tag{1c}$$

$$\frac{\partial (\rho J_i)}{\partial t} + \frac{\partial (\rho J_i v_k + T\delta_{ik})}{\partial x_k} = -\frac{\rho H_i}{\theta_2(\tau_2)} \tag{1d}$$

$$\frac{\partial (\rho E)}{\partial t} + \frac{\partial (\rho E v_k + (p\delta_{ik} - \sigma_{ik}) v_i + q_k)}{\partial x_k} = 0 \tag{1e}$$

where θ_1 and θ_2 are positive scalar functions, and $\psi = \frac{\partial E}{\partial A}$ and $H = \frac{\partial E}{\partial J}$. Note that (1a), (1b), (1c), (1d), (1e) can be written in the following form:

$$\frac{\partial Q}{\partial t} + \nabla \cdot F + B \cdot \nabla Q = S \tag{2}$$

The following definitions are given:

$$p = \rho^2 \frac{\partial E}{\partial \rho} \tag{3a}$$

$$\sigma = -\rho A^T \frac{\partial E}{\partial A} \tag{3b}$$

$$T = \frac{\partial E}{\partial s} \tag{3c}$$

$$q = \frac{\partial E}{\partial s} \frac{\partial E}{\partial J} \tag{3d}$$

To close the system, the EOS must be specified, from which the above quantities and the sources can be derived. E is the sum of the contributions of the energies at the molecular scale (microscale), the material element[1] scale (mesoscale), and the flow scale (macroscale):

$$E = E_1(\rho, s) + E_2(A, J) + E_3(v) \tag{4}$$

In this study, E_1 is taken to correspond to an ideal or stiffened gas:

$$E_1 = \frac{p + \gamma p_\infty}{(\gamma - 1)\rho} \tag{5}$$

where $p_\infty = 0$ for an ideal gas. The temperature is given by:

---

[1]The concept of a *material element* corresponds to that of a fluid parcel from fluid dynamics, applied to both fluids and solids.

$$T = \frac{p + p_\infty}{(\gamma - 1)\, c_v \rho} \tag{6}$$

and the speed of sound by:

$$c_0 = \sqrt{\frac{\gamma\,(p + p_\infty)}{\rho}} \tag{7}$$

It should be noted that there are many other choices that can be made for E_1, dependent on the type of material being modelled.

E_2 is chosen to have the following quadratic form:

$$E_2 = \frac{c_s^2}{4}\, \|\mathrm{dev}\,(G)\|_F^2 + \frac{\alpha^2}{2}\, \|\boldsymbol{J}\|^2 \tag{8}$$

α is a constant related to the characteristic velocity of propagation of heat waves:

$$c_h = \frac{\alpha}{\rho} \sqrt{\frac{T}{c_v}} \tag{9}$$

$G = A^T A$ is the Gramian matrix of the distortion tensor, and $\mathrm{dev}\,(G)$ is the deviator (trace-free part) of G:

$$\mathrm{dev}\,(G) = G - \frac{1}{3}\,\mathrm{tr}\,(G)\,I \tag{10}$$

E_3 is the usual specific kinetic energy per unit mass:

$$E_3 = \frac{1}{2}\,\|\boldsymbol{v}\|^2 \tag{11}$$

The following forms are chosen:

$$\begin{cases} \theta_1\,(\tau_1) = \frac{\tau_1 c_s^2}{3|A|^{\frac{5}{3}}} & \tau_1 = \frac{6\mu}{\rho_0 c_s^2} \\ \theta_2\,(\tau_2) = \tau_2 \alpha^2 \frac{\rho T_0}{\rho_0 T} & \tau_2 = \frac{\rho_0 \kappa}{T_0 \alpha^2} \end{cases} \tag{12}$$

The justification of these choices is that classical Navier–Stokes–Fourier theory is recovered in the stiff limit $\tau_1, \tau_2 \to 0$ [10]. This results in the following relations:

$$\sigma = -\rho c_s^2 G\,\mathrm{dev}\,(G) \tag{13a}$$

$$\boldsymbol{q} = \alpha^2 T \boldsymbol{J} \tag{13b}$$

$$-\frac{\psi}{\theta_1(\tau_1)} = -\frac{3}{\tau_1}\,|A|^{\frac{5}{3}}\,A\,\mathrm{dev}\,(G) \tag{13c}$$

$$-\frac{\rho \boldsymbol{H}}{\theta_2(\tau_2)} = -\frac{T \rho_0}{T_0 \tau_2}\,\boldsymbol{J} \tag{13d}$$

The following constraint also holds [29]:

$$\det\,(A) = \frac{\rho}{\rho_0} \tag{14}$$

The model as presented here is the same in structure as Godunov and Romenski's 1970s model of elastoplastic deformation [16]. The differences between the two models lie in the in the interpretation of the equations in the GPR framework as those governing an arbitrary continuum - not just a solid - and the inclusion of thermal conduction by the evolution of $\boldsymbol{J}$. Unlike in previous continuum models, material elements have not only finite size, but also internal structure.

The strain dissipation time τ_1 of the GPR model is a continuous analogue of Frenkel's "particle settled life time" [13]; the characteristic time taken for a particle to move by a distance of the same order of magnitude as the particle's size. Thus, τ_1 characterizes the time taken for a material element to rearrange with its neighbors. $\tau_1 = \infty$ for solids and $\tau_1 = 0$ for inviscid fluids. It is in this way that the GPR model seeks to describe all three major phases of matter, as long as a continuum description is appropriate for the material at hand.

The evolution equation for $\boldsymbol{J}$ and its contribution to the energy of the system are derived from Romenski's model of hyperbolic heat transfer, originally proposed in [24, 33] and implemented in [32, 31]. In this model, $\boldsymbol{J}$ is effectively defined as the variable conjugate to the entropy flux, in the sense that the latter is the derivative of the specific internal energy with respect to $\boldsymbol{J}$. Romenski remarks that it is more convenient to evolve $\boldsymbol{J}$ and E than the heat flux or the entropy flux, and thus the equations take the form given here. $\boldsymbol{J}$ can intuitively be thought of as a thermal analogue of momentum. τ_2 characterizes the speed of relaxation of the thermal impulse due to heat exchange between material elements.

1.3. Ghost Fluid Methods

Ghost fluid methods, combined with level set methods, are used to model the evolution of interfaces between different materials. They are detailed here, as it is with such a method that this study proposes to model the interfaces between different materials described by the GPR model.

1.3.1. Level Set Methods

Given a function f on $\mathbb{R}$, the level set of f at level c is defined as:

$$\Gamma_c = \{x : f(x) = c\} \tag{15}$$

Given velocity field $v : \mathbb{R} \to \mathbb{R}$, f is advected according to the level set equation [28]:

$$\frac{\partial f}{\partial t} = v\left|\frac{\partial f}{\partial x}\right| \tag{16}$$

The advection of a point in a fluid with velocity v can be modeled by taking $f = x - x_0$ where x_0 is the position of the point at time $t = 0$, and tracking Γ_0. (16) is solved by an appropriate numerical method. The numerical methods used in this study are
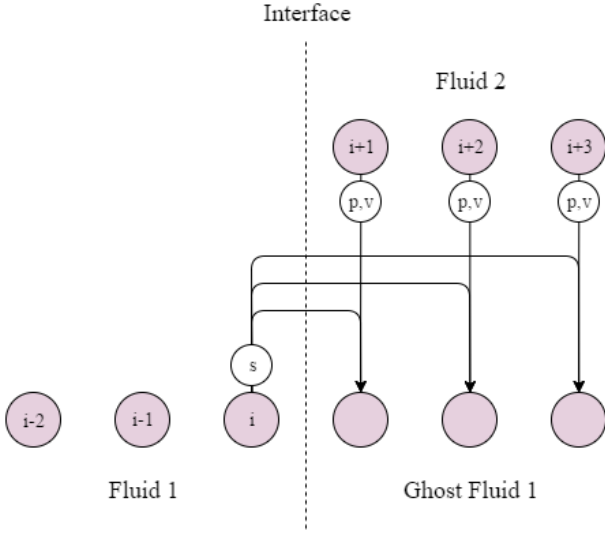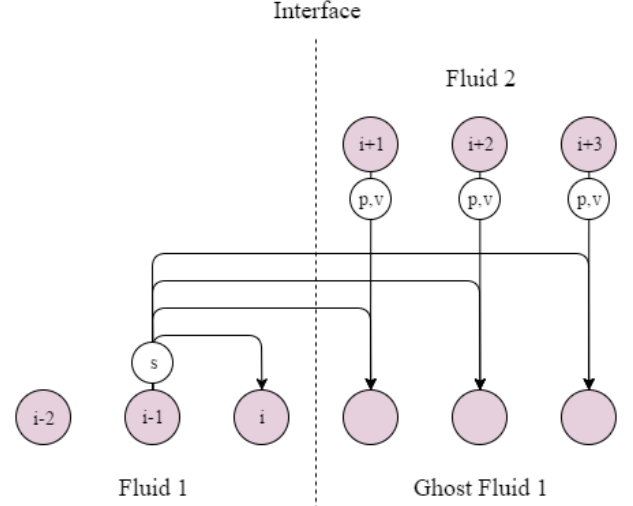
Figure 1: The Original Ghost Fluid Method

Figure 2: The Original Ghost Fluid Method, with the isobaric fix

described in Chapter 2. f will usually have to be renormalized to resemble a straight line at every time step, to avoid unwanted distortions such as becoming a multivalued function.

1.3.2. The Original Ghost Fluid Method

The Original Ghost Fluid Method of Fedkiw et al. [11] (an adaptation of the work of Glimm et al. [15]) is a numerical method for the Euler equations for simulating interfaces between multiple materials. The primitive variables for the Euler equations in 1D are given by $\boldsymbol{P} = \begin{pmatrix} \rho & v & p \end{pmatrix}^T$.

Suppose the interface between two fluids is modeled on spatial domain [0, 1], divided into N cells with width $\Delta x = \frac{1}{N}$. Let the time step be Δt and let $\boldsymbol{P}_i^n$ be the set of primitive variables in cell i at time $t_n = n\Delta t$. Let the level set function f have root x_n where $x_n \in \left[\left(i + \frac{1}{2} \right) \Delta x, \left(i + \frac{3}{2} \right) \Delta x \right]$. Thus, at time t_n the interface lies between the cells with primitive variables $\boldsymbol{P}_i^n, \boldsymbol{P}_{i+1}^n$. Define two sets of primitive variables:

$$\boldsymbol{P}_j^{(1)} = \begin{cases} \boldsymbol{P}_j^n & j \leq i \\ \begin{pmatrix} \rho \left(s_i^n, p_j^n, \gamma_i^n \right) & v_j^n & p_j^n \end{pmatrix} & j > i \end{cases} \quad (17)$$

$$\boldsymbol{P}_j^{(2)} = \begin{cases} \boldsymbol{P}_j^n & j \geq i + 1 \\ \begin{pmatrix} \rho \left(s_{i+1}^n, p_j^n, \gamma_{i+1}^n \right) & v_j^n & p_j^n \end{pmatrix} & j < i + 1 \end{cases} \quad (18)$$

where:

$$\rho \left(s, p, \gamma \right) = \left(\frac{p}{s} \right)^{\frac{1}{\gamma}} \quad (19)$$

All cells in $\boldsymbol{P}^{(1)}$ to the left of the interface have the same state variables as those of $\boldsymbol{P}^n$. All cells to the right have the same

pressure and velocity as their counterparts in $\boldsymbol{P}^n$, but the same entropy as $\boldsymbol{P}_i^n$. This affects their density. The situation is analogous for $\boldsymbol{P}^{(2)}$. This is demonstrated in Figure 1 on page 4.

$\boldsymbol{P}^{(1)}, \boldsymbol{P}^{(2)}$ are stepped forward by time step Δt using a standard Eulerian method. f is advected using (16), taking the velocity in each cell to be that of $\boldsymbol{P}^n$. Now let $f(x_{n+1}) = 0$ where $x_{n+1} \in \left[\left(k + \frac{1}{2} \right) \Delta x, \left(k + \frac{3}{2} \right) \Delta x \right]$ for some k. Define:

$$\boldsymbol{P}_j^{n+1} = \begin{cases} \boldsymbol{P}_j^{(1)} & j \leq k \\ \boldsymbol{P}_j^{(2)} & j > k \end{cases} \quad (20)$$

The rationale behind the original GFM is that in most applications, pressure and velocity are continuous across the interface, and thus the ghost cells may take the real pressure and velocity values. Entropy is generally discontinuous at a contact discontinuity, resulting in large truncation errors if a standard finite difference scheme is used to solve the system. Thus, entropy is extrapolated as a constant from the interface boundary cell into the ghost region.

Fedkiw et al. advised to use the *isobaric fix* technique. This involves setting the entropy of cell i, and all cells in the right ghost region, to that of cell $i - 1$, and setting the entropy of cell $i + 1$, and all cells in the left ghost region, to that of cell $i + 2$. This is demonstrated in Figure 2 on page 4.

Effectively, the ghost regions behave like they are composed of the same fluid as the regions they extend (as they have the same entropy), facilitating calculation of the next time step, but they have the same pressure and velocity profiles as the real fluids they replace, meaning the boundary conditions at the interface are upheld.
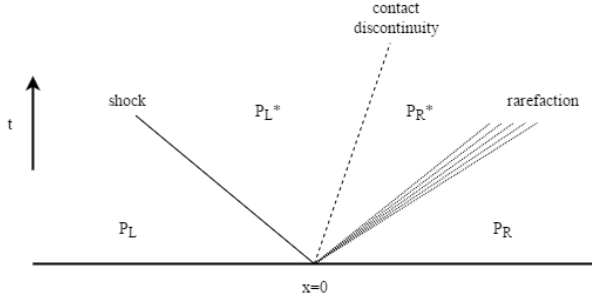
Figure 3: The qualitative structure of the solution to the Riemann Problem, showing the different possible types of waves

1.3.3. The Riemann Ghost Fluid Method

The Riemann Problem in its general form is the solution of the following initial value problem. Given a set of variables P dependent on space and time, and a hyperbolic set of equations which govern their spatio-temporal evolution, $P(x, t)$ is sought for $t > 0$, given the initial condition:

$$P(x, 0) = \begin{cases} P_L & x < 0 \\ P_R & x > 0 \end{cases} \tag{21}$$

This problem is denoted by $RP(P_L, P_R)$. Exact solvers exist for the Riemann Problem for various sets of governing equations, such as the Euler equations [39], the equations of non-linear elasticity [4], or the shallow water equations [2], among others. There also exist approximate solvers for general conservative [27, 23] or non-conservative [8] hyperbolic systems of PDEs. The references given here form a very small sample of the work that has been done in this area.

The solution of the Riemann Problem usually takes the form of a set of waves, between which P is constant. The waves can either be a contact discontinuity (across which pressure and velocity are continuous), a shock (across which all variables may be discontinuous), or a rarefaction (along which the variables vary continuously between their values on either side of the wave). The number and form of the waves are determined by the governing equations and the initial conditions. The states of the variables either side of the contact discontinuity in the middle are known as the *star states*. This qualitative description is depicted in Figure 3 on page 5.

Liu et al. [22] demonstrated that the original GFM fails to resolve strong shocks at material interfaces. This is because the method effectively solves two separate single-fluid Riemann problems. The waves present in these Riemann problems do not necessarily correspond to those in the real Riemann problem across the interface. The Riemann Ghost Fluid Method of Sambasivan et al. [36] aims to rectify this.

Given P^n and $x_n \in \left[\left(i + \frac{1}{2}\right)\Delta x, \left(i + \frac{3}{2}\right)\Delta x\right]$, the ghost cells for fluid 1 are populated with the left star state of $RP\left(P_{i-1}^n, P_{i+2}^n\right)$, and the ghost cells for fluid 2 are populated with the right star
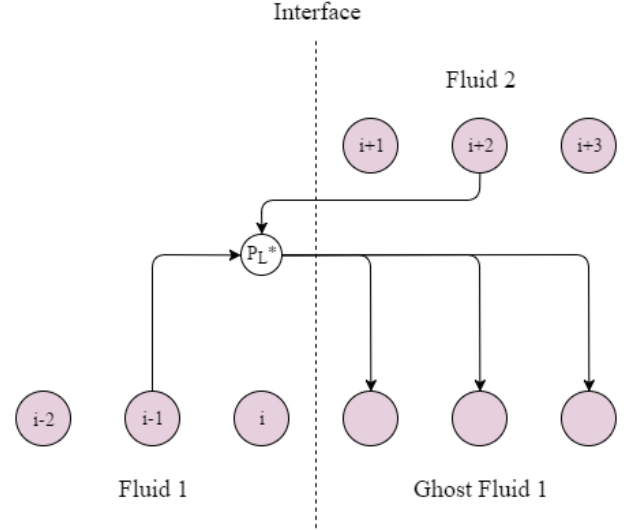
Figure 4: The Riemann Ghost Fluid Method

state. $RP\left(P_{i-1}^n, P_{i+2}^n\right)$ is solved rather than $RP\left(P_i^n, P_{i+1}^n\right)$, as P_i^n, P_{i+1}^n often contain errors generated by the fact that they lie on the material interface. P^{n+1} is then generated as before from the newly formed $P^{(1)}, P^{(2)}$. This process is demonstrated in Figure 4 on page 5.

2. A Riemann Ghost Fluid Method for the GPR Model

2.1. Eigenstructure of the GPR Model

2.1.1. Eigenvalues

Considering the primitive system matrix M_1 given in Section 6, it is clear that the eigenvalues of the GPR system in the first spatial axis consist of v_1 repeated 8 times, along with the roots of:

$$\begin{vmatrix} (v_1 - \lambda)I & \Xi_2 \\ \Xi_1 & (v_1 - \lambda)I \end{vmatrix} = 0 \tag{22}$$

where

$$\Xi_1 = \begin{pmatrix} -\frac{\sigma_{11}}{\rho^2} & \frac{1}{\rho} & -\frac{1}{\rho}\frac{\partial\sigma_{11}}{\partial A_{11}} & -\frac{1}{\rho}\frac{\partial\sigma_{11}}{\partial A_{21}} & -\frac{1}{\rho}\frac{\partial\sigma_{11}}{\partial A_{31}} \\ -\frac{\sigma_{21}}{\rho^2} & 0 & -\frac{1}{\rho}\frac{\partial\sigma_{21}}{\partial A_{11}} & -\frac{1}{\rho}\frac{\partial\sigma_{21}}{\partial A_{21}} & -\frac{1}{\rho}\frac{\partial\sigma_{21}}{\partial A_{31}} \\ -\frac{\sigma_{31}}{\rho^2} & 0 & -\frac{1}{\rho}\frac{\partial\sigma_{31}}{\partial A_{11}} & -\frac{1}{\rho}\frac{\partial\sigma_{31}}{\partial A_{21}} & -\frac{1}{\rho}\frac{\partial\sigma_{31}}{\partial A_{31}} \\ \frac{T_\rho}{\rho} & \frac{T_p}{\rho} & 0 & 0 & 0 \end{pmatrix} \tag{23}$$

$$\Xi_2 = \begin{pmatrix} \rho & 0 & 0 & 0 \\ \rho c_0^2 & 0 & 0 & \frac{\rho c_h^2}{T_p} \\ A_{11} & A_{12} & A_{13} & 0 \\ A_{21} & A_{22} & A_{23} & 0 \\ A_{31} & A_{32} & A_{33} & 0 \end{pmatrix} \tag{24}$$

By the properties of block matrices[2], the remaining eigenvalues are v_1 and the roots of $\left|(v_1 - \lambda)^2 I - \Xi_1 \Xi_2\right| = 0$. Thus, $\lambda_i = v_1 \pm \sqrt{\tilde{\lambda}_i}$ where the $\tilde{\lambda}_i$ are the eigenvalues of the following matrix:

$$\Xi = \Xi_1 \Xi_2 = \begin{pmatrix} \Omega_{11}^1 + c_0^2 & \Omega_{12}^1 & \Omega_{13}^1 & \frac{c_h^2}{T_p} \\ \Omega_{21}^1 & \Omega_{22}^1 & \Omega_{23}^1 & 0 \\ \Omega_{31}^1 & \Omega_{32}^1 & \Omega_{33}^1 & 0 \\ T_\rho + T_p c_0^2 & 0 & 0 & c_h^2 \end{pmatrix} \quad (25)$$

where Ω is given in the next section. Similar results hold for the other two spatial directions. In general it is not possible to express the eigenvalues of Ξ in terms of the eigenvalues of its submatrices. Note, however, that if $\alpha = 0$ then one of the eigenvalues is 0 and the remaining eigenvalues can be found analytically, using the form given in the appendix of [10].

2.1.2. The Acoustic Tensor

It is straightforward to verify the following:

$$\frac{\partial \sigma_{ij}}{\partial A_{mn}} = -c_s^2 \rho \begin{pmatrix} \delta_{in} \left(A \operatorname{dev}(G)\right)_{mj} + \delta_{jn} \left(A \operatorname{dev}(G)\right)_{mi} \\ + A_{mi} G_{jn} + A_{mj} G_{in} - \frac{2}{3} G_{ij} A_{mn} \end{pmatrix} \quad (26)$$

The quantity Ω is named here the *acoustic tensor*, due to its similarity to the acoustic tensor described in [4]:

$$\begin{aligned}
\Omega_{ij}^d &= -\frac{1}{\rho} \frac{\partial \sigma_{id}}{\partial A_{kd}} A_{kj} - \frac{\sigma_{id}}{\rho} \delta_{dj} \quad (27) \\
&= c_s^2 \begin{pmatrix} \delta_{id} \left(G \operatorname{dev}(G)\right)_{dj} + \left(G \operatorname{dev}(G)\right)_{id} \delta_{dj} \\ + \left(G \operatorname{dev}(G)\right)_{ij} + G_{ij} G_{dd} + \frac{1}{3} G_{dj} G_{id} \end{pmatrix} \\
&= c_s^2 \left(E^d G \operatorname{dev}(G) + G \operatorname{dev}(G) E^d + G \operatorname{dev}(G) + G_{dd} G + \frac{1}{3} G_d G_d^T \right)
\end{aligned}$$

where $E_{ij}^d = \delta_{id} \delta_{jd}$.

2.1.3. Eigenvectors

By hyperbolicity of the system, Ξ can be expressed as:

$$\Xi = Q^{-1} D^2 Q \quad (28)$$

where D is a diagonal matrix with positive diagonal entries. The eigenvectors corresponding to $\lambda_i = v_1 \pm \sqrt{\tilde{\lambda}_i}$ take the form $\begin{pmatrix} \boldsymbol{u_1} & \boldsymbol{0_6} & \boldsymbol{u_2} & \boldsymbol{0_2} \end{pmatrix}^T$ where $\boldsymbol{u_1} \in \mathbb{R}^5$, $\boldsymbol{u_2} \in \mathbb{R}^4$ satisfy:

$$\begin{pmatrix} v_1 I & \Xi_2 \\ \Xi_1 & v_1 I \end{pmatrix} \begin{pmatrix} \boldsymbol{u_1} \\ \boldsymbol{u_2} \end{pmatrix} = \left(v_1 \pm \sqrt{\tilde{\lambda}_i} \right) \begin{pmatrix} \boldsymbol{u_1} \\ \boldsymbol{u_2} \end{pmatrix} \quad (29)$$

---

[2]If A is invertible, $\det \begin{pmatrix} A & B \\ C & D \end{pmatrix} = \det(A) \det\left(D - CA^{-1}B\right)$
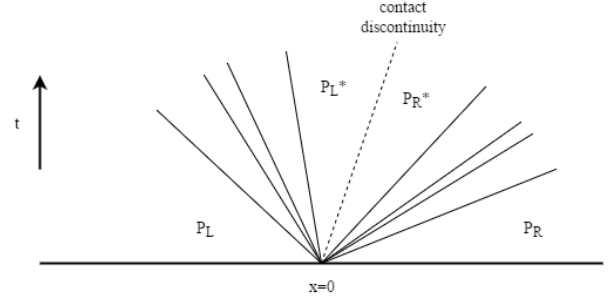
Figure 5: The Riemann Problem for the GPR model, assuming all waves are distinct

Thus, $\Xi_2 \boldsymbol{u_2} = \pm \sqrt{\tilde{\lambda}_i} \boldsymbol{u_1}$ and $\Xi_1 \boldsymbol{u_1} = \pm \sqrt{\tilde{\lambda}_i} \boldsymbol{u_2}$. Combining these results, $\Xi \boldsymbol{u_2} = \tilde{\lambda}_i \boldsymbol{u_2}$. Thus, $\boldsymbol{u_2}$ is a right eigenvector of Ξ and, taking the form $Q^{-1} \boldsymbol{e_i}$ for some $i = 1 \ldots 4$.

Let $\Pi_k^{ij} = \frac{\partial \sigma_{i1}}{\partial A_{jk}}$. Using the result just obtained, the four eigenvectors corresponding to eigenvalues of the form $v_1 + \sqrt{\tilde{\lambda}_i}$ are columns 1-4 of matrix R in (39). Those corresponding to eigenvalues of the form $v_1 - \sqrt{\tilde{\lambda}_i}$ are columns 5-8. By inspection, it can be verified that the remaining 9 eigenvectors (corresponding to eigenvalue v_1) are the remaining columns.

A similar analysis yields the left eigenvectors as the rows of (41). In the form given here, $L = R^{-1}$.

2.2. A GPR Riemann Ghost Fluid Method

Barton et al. have presented an RGFM for the equations of non-linear elasticity [5, 3]. Owing to the similarity of the structure of the non-linear elasticity equations to those of the GPR model (differing only in the presence of source terms and the form of the shear stress tensor, and possibly the EOS), their method is built upon here. The resulting method is named *the GPR-RGFM*.

The Riemann Problem of the GPR model takes the form demonstrated in Figure 5 on page 6. Assuming all waves are distinct, there are four waves on either side of the contact discontinuity. On each side, one wave corresponds to the thermal impulse (manifesting as a heat wave) and the other three correspond to the distortion components in the axis in which the Riemann Problem is considered (manifesting as two shear waves and one longitudinal pressure wave). In the following the effect of the source terms on the solution to the RP is neglected. This is thought to be a reasonable assumption for the problem at hand, as only the star states are required, and the time step over which the RP is taken is very small. The method is presented here along the first spatial axis. It can easily be adapted along any axis.

Denote the vector of primitive variables by $\boldsymbol{P}$. Take the set of left eigenvectors L (41) with eigenvalues $\{\lambda_i\}$. Neglecting the effect of the source terms produces the standard set of relations
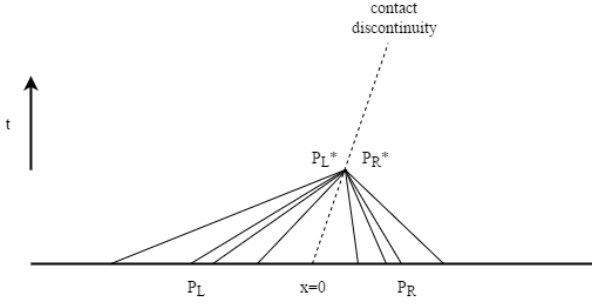
Figure 6: Different sets of characteristic curves, traveling from their respective initial points to the star region

along characteristics (curves along which $\frac{dx}{dt} = \lambda_i$):[3]

$$L \cdot d\boldsymbol{P} = dt \cdot L \cdot \boldsymbol{S} \tag{30}$$

$\boldsymbol{P}^*_K$ is now sought, where $K = L$ or $K = R$, denoting the left or right sides of the interface, respectively. Take the following linearisation:

$$d\boldsymbol{P} \approx \boldsymbol{P}^*_K - \boldsymbol{P}_K \tag{31}$$

13 relations from (30) are taken: four regarding the 4 sets of characteristics traveling into the contact discontinuity from side K (with speeds greater or less than v for $K = L$ or $K = R$, respectively), and nine relating to the contact discontinuity itself. This is demonstrated in Figure 6 on page 7. Four more relations must be derived to solve the system for $\boldsymbol{P}^*_K$. Expanding the Taylor series of $\boldsymbol{\Sigma}^*_1, T^*$:

$$\boldsymbol{\Sigma}^*_1 = \boldsymbol{\Sigma}_1 + \frac{\partial \boldsymbol{\Sigma}_1}{\partial \rho} (\rho^* - \rho) + \frac{\partial \boldsymbol{\Sigma}_1}{\partial p} (p^* - p) \tag{32a}$$

$$+ \frac{\partial \boldsymbol{\Sigma}_1}{\partial A_{mn}} (A^*_{mn} - A_{mn}) + H.O.T.$$

$$T^* = T + \frac{\partial T}{\partial \rho} (\rho^* - \rho) + \frac{\partial T}{\partial p} (p^* - p) + H.O.T. \tag{32b}$$

Thus, we have:

[3]Take the hyperbolic system $\frac{\partial \boldsymbol{P}}{\partial t} + M \frac{\partial \boldsymbol{P}}{\partial x} = \boldsymbol{S}$. Let $\boldsymbol{l_i}^T M = \lambda_i \boldsymbol{l_i}^T$. Along characteristics corresponding to λ_i:

$$\boldsymbol{l}_i^T \left(\frac{\partial \boldsymbol{P}}{\partial t} + M \frac{\partial \boldsymbol{P}}{\partial x} \right) = \boldsymbol{l}_i^T \left(\frac{\partial \boldsymbol{P}}{\partial t} + \frac{dx}{dt} \frac{\partial \boldsymbol{P}}{\partial x} \right)$$

$$= \boldsymbol{l}_i^T \frac{d\boldsymbol{P}}{dt} = \boldsymbol{l}_i^T \boldsymbol{S}$$

$$\boldsymbol{\Sigma}^*_1 - \boldsymbol{\Sigma}_1 \approx -\frac{\boldsymbol{\sigma}_1}{\rho} (\rho^* - \rho) + \boldsymbol{e}_1 (p^* - p) \tag{33a}$$

$$- \frac{\partial \boldsymbol{\sigma}_1}{\partial A_{mn}} (A^*_{mn} - A_{mn})$$

$$T^* - T \approx -\frac{T}{\rho} (\rho^* - \rho) + \frac{T}{p + p_\infty} (p^* - p) \tag{33b}$$

These are the extra required relations. Thus:

$$\hat{L}_K \cdot \left(\boldsymbol{P}^*_K - \boldsymbol{P}_K \right) = \boldsymbol{c}_K \tag{34}$$

where $\hat{L}_K$ takes the form found in (43), with $\xi = -1$ for $K = R$ and $\xi = 1$ for $K = L$, and:

$$\boldsymbol{c}_K = \begin{pmatrix} \left(\boldsymbol{\Sigma}^*_1 \right)_K - (\boldsymbol{\Sigma}_1)_K \\ T^*_K - T_K \\ dt \cdot (L_K \cdot \boldsymbol{S}_K)_{5:17} \end{pmatrix} \tag{35}$$

The inverse of $\hat{L}_K$ takes the form found in (44).

$\hat{L}_K, \hat{L}^{-1}_K$ are evaluated at $\boldsymbol{P}_K$. It remains to find expressions for $\boldsymbol{\Sigma}^*_1$ and T^* in terms of $\boldsymbol{P}_L, \boldsymbol{P}_R$ to close the system. The following boundary conditions are used:

$$\left(\boldsymbol{\Sigma}^*_1 \right)_L = \left(\boldsymbol{\Sigma}^*_1 \right)_R \tag{36a}$$

$$T^*_L = T^*_R \tag{36b}$$

$$\boldsymbol{v}^*_L = \boldsymbol{v}^*_R \tag{36c}$$

$$(J_1)^*_L = (J_1)^*_R \tag{36d}$$

Taking the relevent rows of $\boldsymbol{P}^*_K = \boldsymbol{P}_K + \hat{L}^{-1}_K \boldsymbol{c}_K$:

$$\begin{pmatrix} \boldsymbol{v}^* \\ J^*_1 \end{pmatrix} = \begin{pmatrix} \boldsymbol{v}_K \\ (J_1)_K \end{pmatrix} + Y_K \left(\begin{pmatrix} \boldsymbol{\Sigma}^*_1 \\ T^* \end{pmatrix} - \begin{pmatrix} (\boldsymbol{\Sigma}_1)_K \\ T_K \end{pmatrix} \right) \tag{37}$$

$$+ dt \cdot \xi_K \cdot Q^{-1}_K (L_K \cdot \boldsymbol{S}_K)_{5:8}$$

Thus, using the boundary conditions:

$$\begin{pmatrix} \boldsymbol{\Sigma}^*_1 \\ T^* \end{pmatrix} = (Y_L - Y_R)^{-1} \left(\begin{array}{c} \begin{pmatrix} \boldsymbol{v}_R \\ (J_1)_R \end{pmatrix} - \begin{pmatrix} \boldsymbol{v}_L \\ (J_1)_L \end{pmatrix} \\ + dt \left(Q^{-1}_R (L_R \cdot \boldsymbol{S}_R)_{5:8} + Q^{-1}_L (L_L \cdot \boldsymbol{S}_L)_{5:8} \right) \\ + Y_L \begin{pmatrix} (\boldsymbol{\Sigma}_1)_L \\ T_L \end{pmatrix} - Y_R \begin{pmatrix} (\boldsymbol{\Sigma}_1)_R \\ T_R \end{pmatrix} \end{array} \right) \tag{38}$$

Thus, $\boldsymbol{P}^*_L, \boldsymbol{P}^*_R$ are obtained with (34) and used in the RGFM, as described in Section 1.3.

It may be necessary to iterate this process a few times to ensure convergence to star states for which the boundary conditions hold.

$$R = \begin{pmatrix} \frac{1}{2}\left(\Xi_2\left(DQ\right)^{-1}\right)_{1,:} & \frac{1}{2}\left(\Xi_2\left(DQ\right)^{-1}\right)_{1,:} & c\rho & 0 & 0 & 0 \\ \frac{1}{2}\left(\Xi_2\left(DQ\right)^{-1}\right)_{2,:} & \frac{1}{2}\left(\Xi_2\left(DQ\right)^{-1}\right)_{2,:} & c\left(p+p_\infty\right) & 0 & 0 & 0 \\ \frac{1}{2}\left(\Xi_2\left(DQ\right)^{-1}\right)_{3:5,:} & \frac{1}{2}\left(\Xi_2\left(DQ\right)^{-1}\right)_{3:5,:} & c\Pi_1^{-1}\boldsymbol{w} & -\Pi_1^{-1}\Pi_2 & -\Pi_1^{-1}\Pi_3 & 0 \\ 0 & 0 & 0 & I_3 & 0 & 0 \\ 0 & 0 & 0 & 0 & I_3 & 0 \\ \frac{1}{2}Q^{-1} & -\frac{1}{2}Q^{-1} & 0 & 0 & 0 & 0 \\ 0 & 0 & 0 & 0 & 0 & I_2 \end{pmatrix} \tag{39}$$

where

$$\boldsymbol{w} = \left(p+p_\infty\right)\boldsymbol{e_1} - \boldsymbol{\sigma_1} \tag{40a}$$

$$c = \frac{1}{\boldsymbol{e_1^T}\left(\Pi_1 A\right)^{-1}\boldsymbol{w} - 1} \tag{40b}$$

Figure 7: Right eigenvectors of primitive GPR system

$$L = \begin{pmatrix} D^{-1}Q\Xi_1 & -\frac{1}{\rho}D^{-1}Q_{1:3}\Pi_2 & -\frac{1}{\rho}D^{-1}Q_{1:3}\Pi_3 & Q & 0 \\ D^{-1}Q\Xi_1 & -\frac{1}{\rho}D^{-1}Q_{1:3}\Pi_2 & -\frac{1}{\rho}D^{-1}Q_{1:3}\Pi_3 & -Q & 0 \\ \boldsymbol{y} & \boldsymbol{e_1^T}A^{-1}\Pi_1^{-1}\Pi_2 & \boldsymbol{e_1^T}A^{-1}\Pi_1^{-1}\Pi_3 & 0 & 0 \\ 0 & I_3 & 0 & 0 & 0 \\ 0 & 0 & I_3 & 0 & 0 \\ 0 & 0 & 0 & 0 & I_2 \end{pmatrix} \tag{41}$$

where

$$\boldsymbol{y} = \begin{pmatrix} -\frac{1}{\rho} & 0 & \boldsymbol{e_1^T}A^{-1} \end{pmatrix} \tag{42}$$

Figure 8: Left eigenvectors of primitive GPR system

$$\hat{L}_K = \begin{pmatrix} -\frac{\sigma_1}{\rho} & \boldsymbol{e_1} & -\Pi_1 & -\Pi_2 & -\Pi_3 & 0 & 0 \\ -\frac{T}{\rho} & \frac{T}{p+p_\infty} & 0 & 0 & 0 & 0 & 0 \\ \left(D^{-1}Q\Xi_1\right)_1 & \left(D^{-1}Q\Xi_1\right)_2 & \left(D^{-1}Q\Xi_1\right)_{3:5} & -\frac{1}{\rho}D^{-1}Q_{1:3}\Pi_2 & -\frac{1}{\rho}D^{-1}Q_{1:3}\Pi_3 & \xi Q & 0 \\ -\frac{1}{\rho} & 0 & \boldsymbol{e_1^T}A^{-1} & \boldsymbol{e_1^T}A^{-1}\Pi_1^{-1}\Pi_2 & \boldsymbol{e_1^T}A^{-1}\Pi_1^{-1}\Pi_3 & 0 & 0 \\ 0 & 0 & 0 & I_3 & 0 & 0 & 0 \\ 0 & 0 & 0 & 0 & I_3 & 0 & 0 \\ 0 & 0 & 0 & 0 & 0 & 0 & I_2 \end{pmatrix} \tag{43}$$

Figure 9: System matrix for linearised solver

$$\hat{L}_K^{-1} = \begin{pmatrix} \boldsymbol{a}^T\rho & 0 & c\rho & 0 & 0 & 0 \\ \boldsymbol{a}^T\,(p+p_\infty) + \frac{p+p_\infty}{T}\boldsymbol{e}_4^T & 0 & c\,(p+p_\infty) & 0 & 0 & 0 \\ X & 0 & c\Pi_1^{-1}\boldsymbol{w} & -\Pi_1^{-1}\Pi_2 & -\Pi_1^{-1}\Pi_3 & 0 \\ 0 & 0 & 0 & I_3 & 0 & 0 \\ 0 & 0 & 0 & 0 & I_3 & 0 \\ Y & \xi Q^{-1} & 0 & 0 & 0 & 0 \\ 0 & 0 & 0 & 0 & 0 & I_2 \end{pmatrix} \tag{44}$$

where:

$$Z_1 = ((p + p_\infty)\,\boldsymbol{e}_1 - \boldsymbol{\sigma}_1)\,\boldsymbol{e}_1^T - \Pi_1 A \tag{45a}$$

$$Z_0 = \begin{pmatrix} 1 & 0 & 0 & -\frac{p+p_\infty}{T} \\ 0 & 1 & 0 & 0 \\ 0 & 0 & 1 & 0 \end{pmatrix} \tag{45b}$$

$$\boldsymbol{a}^T = \boldsymbol{e}_1^T Z_1^{-1} Z_0 \tag{45c}$$

$$X = A Z_1^{-1} Z_0 \tag{45d}$$

$$Y = -\xi Q^{-1} D^{-1} Q \Xi_1 \begin{pmatrix} \boldsymbol{a}^T\rho \\ \boldsymbol{a}^T\,(p+p_\infty) + \frac{p+p_\infty}{T}\boldsymbol{e}_4^T \\ X \end{pmatrix} \tag{45e}$$

Figure 10: Inverse of system matrix for linearised solver

3. Results

The GPR-RGFM is now assessed. The first two tests in this chapter are standard Riemann problems, exact solutions to which exist for the Euler equations. The viscosity of the GPR model smears the solutions in areas in which the solutions to the Euler equations are discontinuous or not smooth. This smearing is not the result of using a low-order solver (all results in these sections being calculated to third order). The last two tests assess the ability of the GPR-RGFM to correctly model heat conduction across interfaces.

3.1. Water-Water Interface

This problem tests the GPR-RGFM for the stiffened EOS. The test comprises two volumes of water with different pressures, meeting at $x = 0.5$ (as found in Ghaisas et al. [14], Test III.B.2). The initial conditions are found in Table 1 on page 9. Realistic values are chosen for the material parameters: $\gamma = 4.4$, $p_\infty = 6 \times 10^8$, $c_v = 950$, $\mu = 10^{-3}$, $P_r = 7$, $\rho_0 = 1000$, $T_0 = 300$. c_s and α are taken to be 55 and 500, respectively. The final time is $t = 1.5 \times 10^{-4}$ and all simulations used 200 cells.

The results in Figure 11 on page 10 without the GPR-RGFM match those in [14] well. The sharp contact discontinuity is preserved by the GPR-RGFM.

3.2. Helium Bubble

The interface between two different gases is now modeled. As in Test B of Wang et al. [40], a bubble of helium - surrounded by air - initially occupies the region $x \in [0.4, 0.6]$. A shock front

	ρ	p	v	A	J
$x < 0.5$	1000	7×10^8	$\boldsymbol{0}$	I_3	$\boldsymbol{0}$
$x \geq 0.5$	1000	10^8	$\boldsymbol{0}$	I_3	$\boldsymbol{0}$

Table 1: Initial conditions for the water-water interface test

in the air, initially at $x = 0.05$, travels towards the helium bubble. The initial conditions are given in Table 2 on page 12. Realistic material parameters are taken for the helium: $\gamma = 1.66$, $c_v = 3127$, $\rho_0 = 0.163$, $\mu = 1.99 \times 10^{-5}$, $P_r = 0.688$, and for the air: $\gamma = 1.4$, $c_v = 721$, $\rho_0 = 1.18$, $\mu = 1.85 \times 10^{-5}$, $P_r = 0.714$. In both cases, $p_0 = 101325$, $c_s = 55$, and $\alpha = 500$.

200 cells are used. The results for times $t = 7 \times 10^{-4}$ and $t = 14 \times 10^{-4}$ are displayed in Figure 12 on page 11. In the former, the shock is about to hit the helium bubble (corresponding to the region of low density). In the latter, the shock has traveled through the helium bubble, compressing it slightly, and the bubble itself has moved almost 0.1 spatial units to the right. There is good correspondence with the results in [40] and the sharp discontinuity in density is maintained.

3.3. Heat Conduction in a Gas

This test is based on the Heat Conduction in a Gas Test of Dumbser et al. [10]. Two ideal gases at different temperatures are initially in contact at position $x = 0$. The initial conditions for this problem are given in Table 3 on page 12.

The material parameters are taken to be: $\gamma = 1.4$, $c_v = 2.5$, $\rho_0 = 1$, $p_0 = 1$, $c_s = 1$, $\alpha = 2$, $\mu = 10^{-2}$, $\kappa = 10^{-2}$. An interface
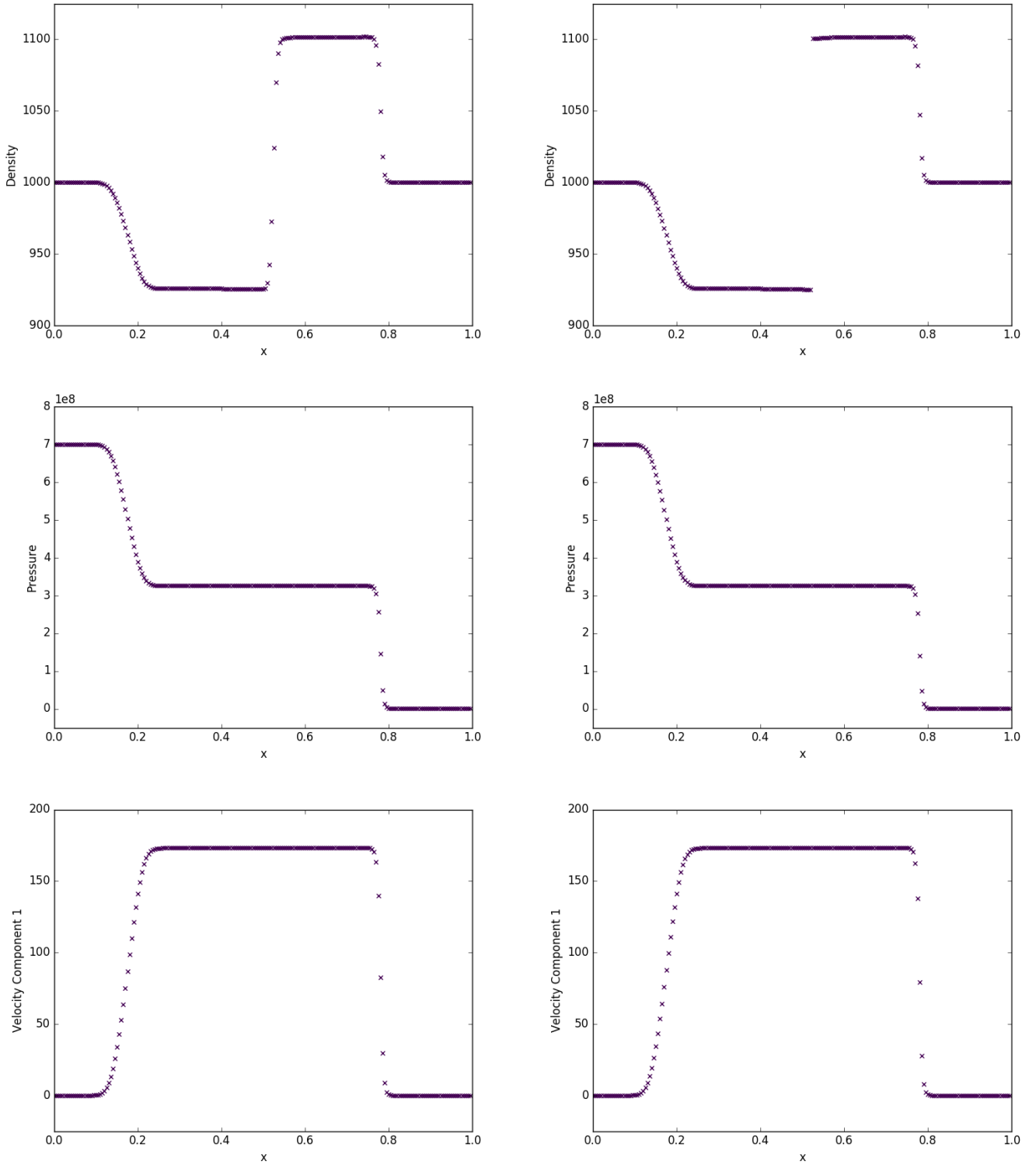
Figure 11: Density, pressure, and velocity for the water-water interface test without GPR-RGFM (left) / with GPR-RGFM (right)
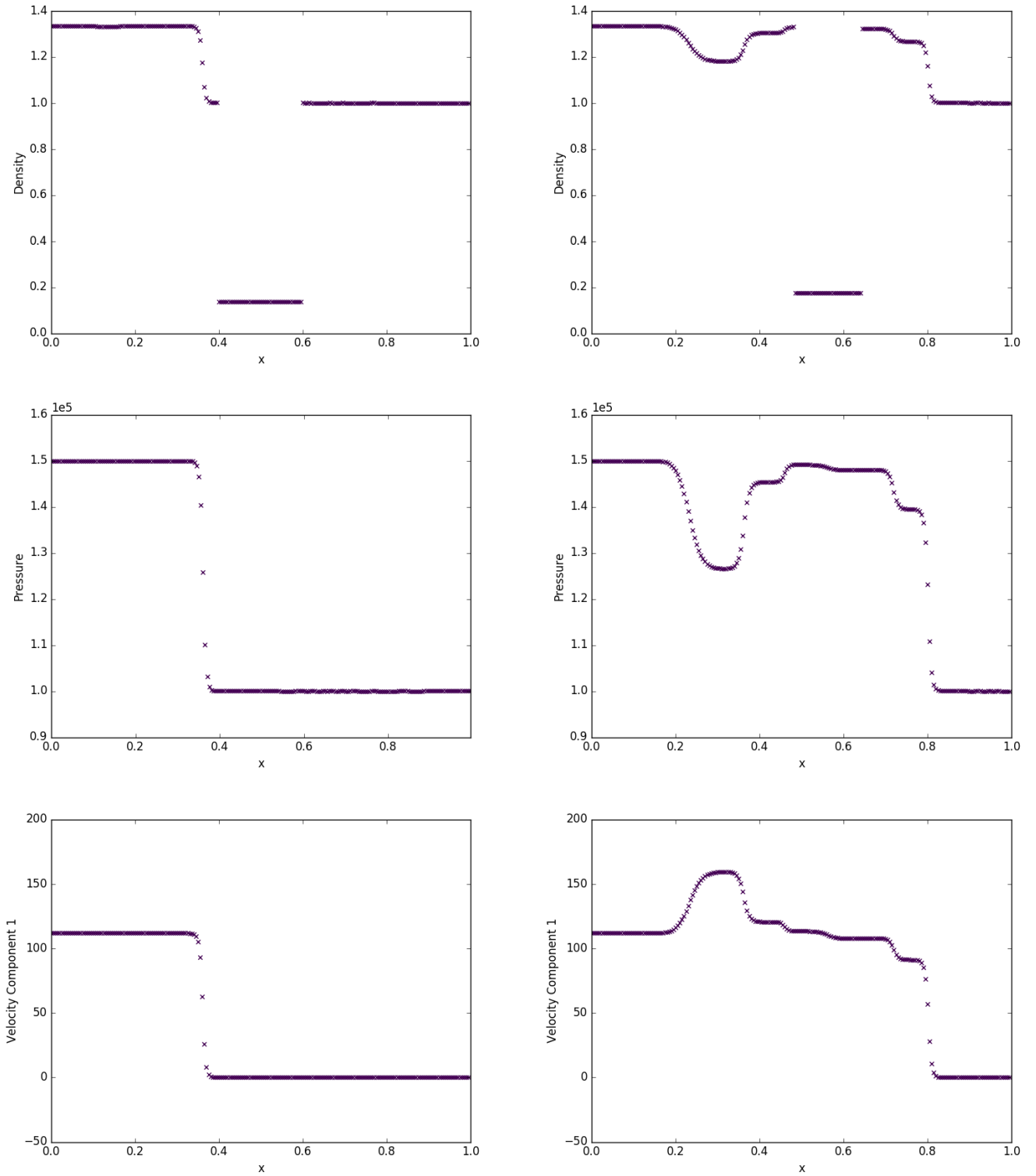
Figure 12: Density, pressure, and velocity for the helium bubble test with GPR-RGFM at times $t = 7 \times 10^{-4}$ (left) and $t = 14 \times 10^{-4}$ (right)

	ρ	p	v	A	J
$x < 0.05$	1.3333	1.5×10^5	$\begin{pmatrix} 35.35\sqrt{10} & 0 & 0 \end{pmatrix}$	$\left(\frac{1.3333}{1.18}\right)^{\frac{1}{3}} I_3$	$\mathbf{0}$
$0.05 \leq x < 0.4$	1	10^5	$\mathbf{0}$	$\left(\frac{1}{1.18}\right)^{\frac{1}{3}} I_3$	$\mathbf{0}$
$0.4 \leq x < 0.6$	0.1379	10^5	$\mathbf{0}$	$\left(\frac{0.1379}{0.163}\right)^{\frac{1}{3}} I_3$	$\mathbf{0}$
$0.6 \leq x \leq 1$	1	10^5	$\mathbf{0}$	$\left(\frac{1}{1.18}\right)^{\frac{1}{3}} I_3$	$\mathbf{0}$

Table 2: Initial conditions for the helium bubble test

	ρ	p	v	A	J
$x < 0$	2	1	$\mathbf{0}$	$\sqrt[3]{2} \cdot I_3$	$\mathbf{0}$
$x \geq 0$	0.5	1	$\mathbf{0}$	$\frac{1}{\sqrt[3]{2}} \cdot I_3$	$\mathbf{0}$

Table 3: Initial conditions for the heat conduction test

	ρ	p	v	A	J
air	1.18	101325	$\mathbf{0}$	I_3	$\mathbf{0}$
helium	0.164	101325	$\mathbf{0}$	I_3	$\mathbf{0}$

Table 4: Initial conditions for the intermaterial heating-induced acoustic wave test

is initially placed between the two volumes of air at $x = 0.5$. The final time is taken to be $t = 1$, and 200 cells are used. Results are displayed in Figure 13 on page 13, using the results from [9] as a reference. The material interface is denoted by a dashed vertical line.

The temperature curve generated using the GPR-RGFM matches very well the reference solution. The interface has moved to $x = 0.53756$, as is to be expected, as the cooler gas on the left expands as it heats up, and the hotter gas on the right contracts as it cools. Initially, the mass of the left volume is 1 and the right volume is 0.25. At $t = 1$, these masses are 0.9997 and 0.2503, respectively. Thus, mass on either side is conserved to a good approximation. Although the GPR-RGFM results for the heat flux match the reference solution well over most of the domain, there are aberrations in a small region around the interface. Although this doesn't affect the temperature curve, these discrepancies are undesirable, and possible methods to rectify them are discussed in 4.2.

3.4. Intermaterial Heating-Induced Acoustic Wave

The test assesses the ability of the GPR-RGFM to conduct heat between two different materials. Take the material parameters for air and helium from Section 3.2. Take the scaled spatial variable x^* defined by:

$$x = \frac{\mu^{air} c_0^{air}}{p_0 \gamma^{air}} x^* \tag{46}$$

The domain $x^* \in [0, 90]$ is used. Thermal energy is added at the left boundary at a high power of $\frac{\gamma^{air} p_0 c_0^{air}}{P_r^{air}(\gamma^{air}-1)}$ (around $1.7 \times 10^8 Wm^{-2}$). Three scenarios are tested:

1. The domain is filled with air.
2. The domain comprises two volumes of air, initially separated at $x^* = 22.5$.

3. The domain comprises a volume of air (left) and a volume of helium (right), initially separated at $x^* = 22.5$.

The initial conditions for the two gases in all scenarios are given in Table 4 on page 12. The results of the test are shown in Figure 14 on page 14 and Figure 15 on page 15 for various times. The material interface is represented by a dashed vertical line in scenarios 2 and 3. All simulations used 400 cells.

As the left wall heats up, a temperature gradient develops and the acoustic wave described appears. The results for scenarios 1 and 2 are indistinguishable, as they should be, and there are no aberrations around the material interface in scenario 2. In scenario 3, the acoustic wave hits the interface at around $t = 2 \times 10^{-9}$ and then speeds up (as it should, the speed of sound in helium being around three times that of air). The heat flux wave increases in intensity after passing into the helium, owing to the fact that the wave is traveling faster. As expected, all variables displayed are continuous across the interface.

In scenarios 2 and 3 the interface moves to the right as the air heats up and expands. The masses of the air volumes in these two scenarios at various times are given in Table 5 on page 16, demonstrating that mass is conserved well as the interface moves.

4. Discussion

Throughout this study, the various fluids have been assumed to be immiscible. Whilst this is a common assumption in situations where mixing is low or practically non-existent, there are many problems which may require it. It should be fairly straightforward to implement a mixture model such as that proposed by Romenski et al. [32, 31], which uses the same thermal conduction system as the GPR model.
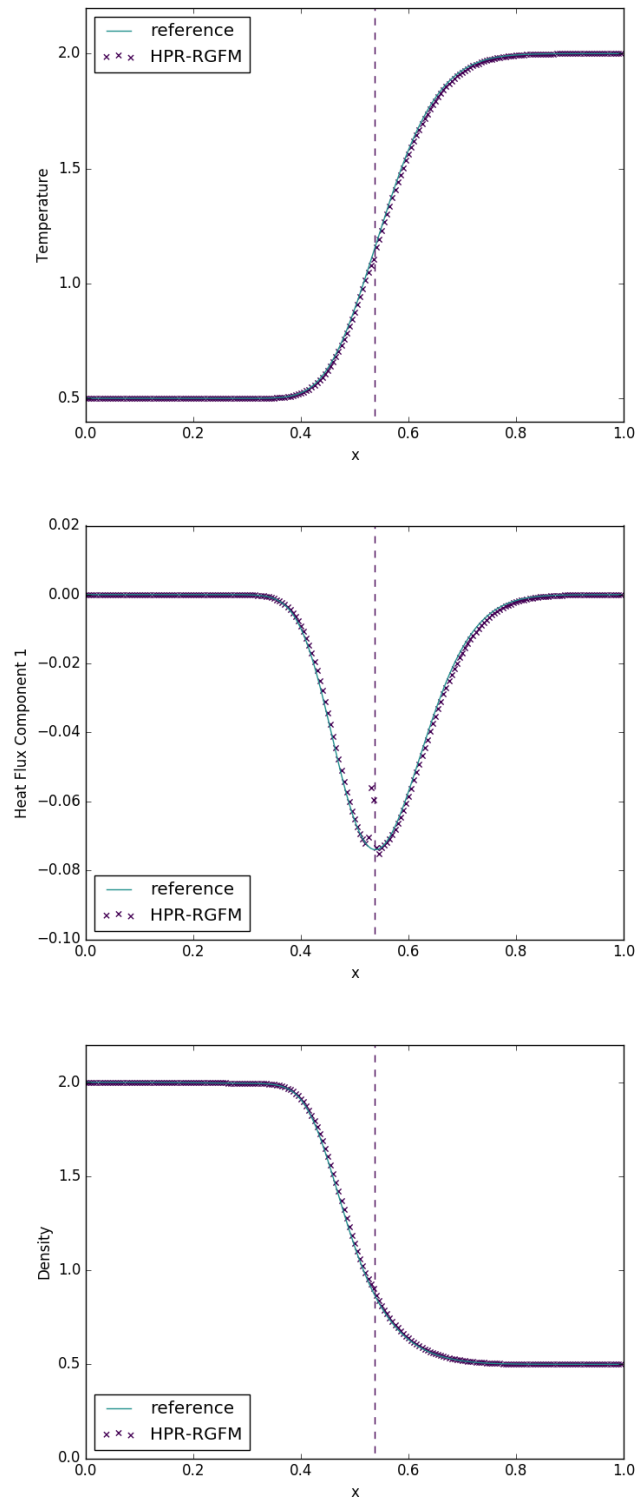
Figure 13: Temperature, heat flux, and density for the intermaterial heat conduction test with GPR-RGFM
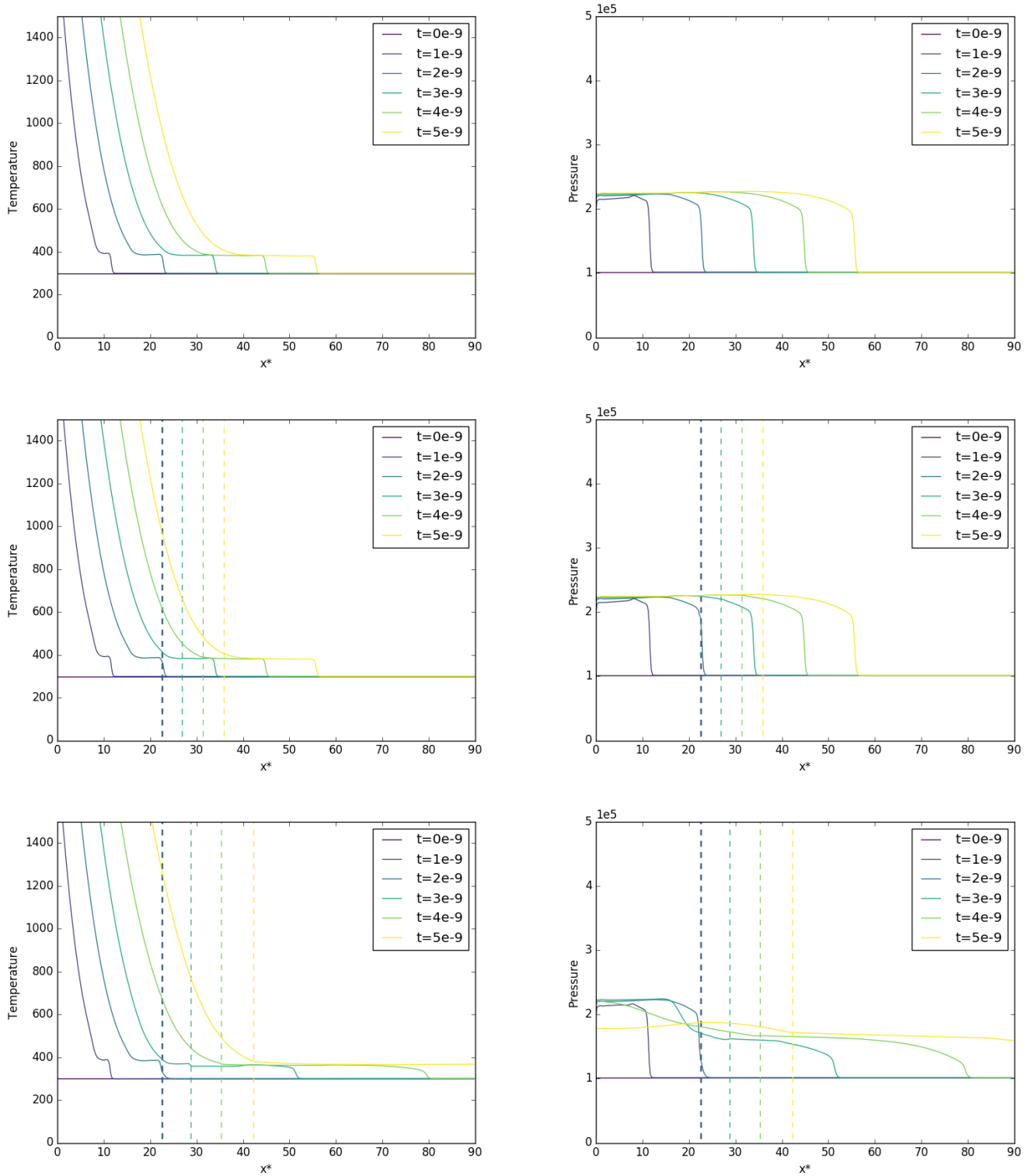
Figure 14: Temperature and pressure for the intermaterial heating-induced acoustic wave test with: a single volume of air (top); two volumes of air initially separated at $x^* = 22.5$ (middle); air and helium initially separated at $x^* = 22.5$ (bottom).
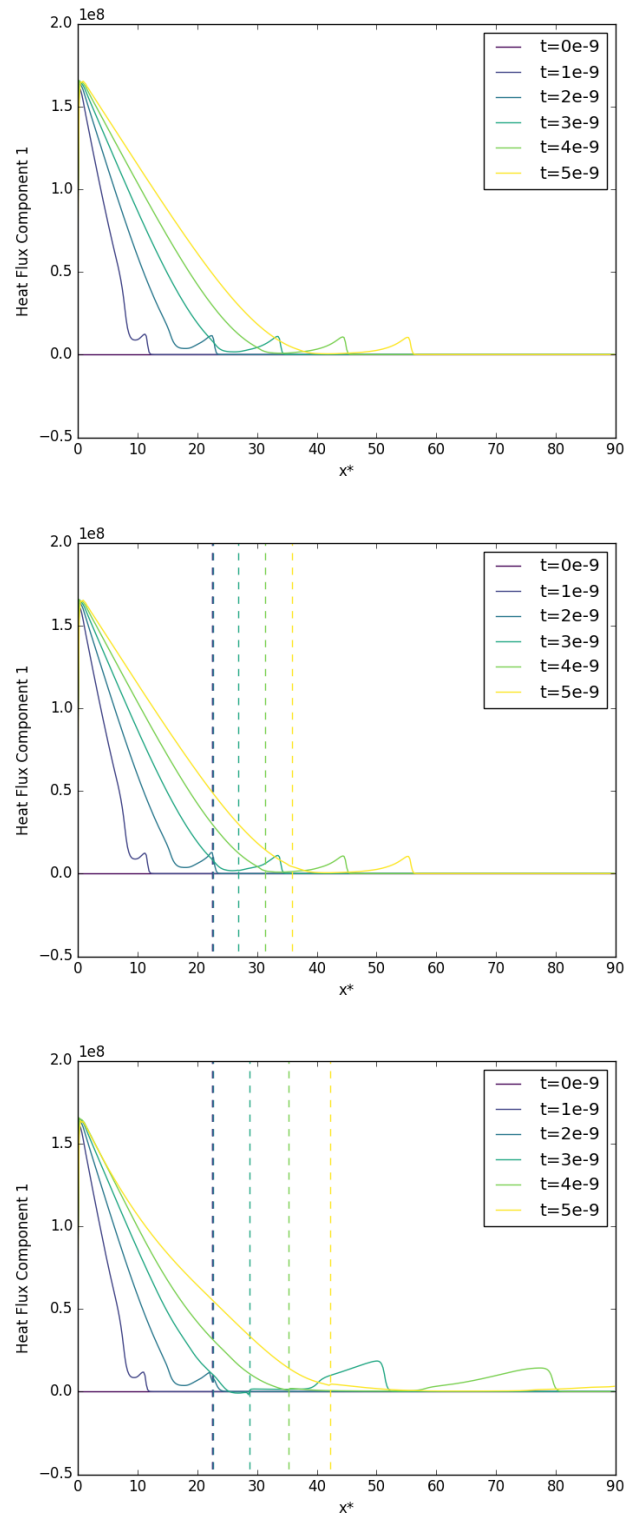
Figure 15: Heat flux for the intermaterial heating-induced acoustic wave test with: a single volume of air (top); two volumes of air initially separated at $x^* = 22.5$ (middle); air and helium initially separated at $x^* = 22.5$ (bottom).

Time ($\times 10^{-9}$)	0	1	2	3	4	5
Mass in Scenario 2 ($\times 10^{-6}$)	1.254	1.255	1.253	1.252	1.252	1.253
Mass in Scenario 3 ($\times 10^{-6}$)	1.254	1.253	1.248	1.254	1.255	1.255

Table 5: Mass of the air volume in scenarios 2 and 3 at various times

The Riemann Ghost Fluid Method presented in Section 2.2 has been demonstrated to be a viable way of accurately simulating the interfaces between different materials described by the GPR model. Unlike in many existing implementations, heat conduction across the interface was simulated accurately. This greatly simplifies the conceptual framework required for multiphase interactions, as described in 1.1. Implementation should be easier and quicker, and future work can be more focused on a single model, rather than several fundamentally different frameworks.

4.1. Limitations

The truncation of the Taylor series expansions (32a) and (32b) used to find the star states of the heat flux and the viscous stress tensor implicitly assumes that there are only small differences between the side states and the star states of the variables upon which q_1^*, σ_1^* depend (ρ, p, J_1, and A_1). If this is the case, higher order terms of the expansion can be neglected. If it is not, however, the method may fail.

The linearised nature of the GPR-RGFM solver also implicitly assumes that all waves of interest present in the Riemann Problem are shocks. Thus, strong rarefactions may cause the method to fail. An example of this is the failure of the GPR-RGFM on the water-gas shock tube test (taken from [7]). The domain $[0, 1]$ is initially occupied on $[0, 0.7]$ by water (with material parameters given in Section 3.1) and on $(0.7, 1]$ by air (with material parameters given in Section 3.2). The water initially has density 1000 and pressure 10^9. The air initially has density 50 and pressure 101325. The exact density and pressure resulting from simulating the problem with the Euler equations to time $t = 237.44 \times 10^{-6}$ are shown in Figure 16 on page 17. The material interface is located at $x = 0.8146$. Note the strong rarefaction on the left, and the large disparity between $p_L = 10^9$ and $p^* \approx 1.4 \times 10^7$, and similarly on the right side with $p_R \approx 10^5$.

4.2. Potential Improvements

An obvious improvement to the GPR-RGFM method presented would be to use a better Riemann solver than the iterative, linearised solver devised in Section 2.2. Let L be the matrix of left eigenvectors of the primitive system. As noted previously, the solver relies upon the fact that each of the following relations holds along the characteristic to which it corresponds:

$$L \cdot \frac{d\boldsymbol{P}}{dt} = L \cdot \boldsymbol{S} \qquad (47)$$

It may be that some numerical method is required to integrate (47) from the left and right interface boundary states to their respective star states.

Alternatively, a completely different approximate Riemann solver could be employed, such as the universal HLLEM solver of Dumbser et al. [8]. This path-conservative formulation of the HLLEM solver works for general non-conservative systems (such as the GPR model) and is simple to implement. It's based upon a new path-conservative HLL method (building on the original method of Harten, Lax, and van Leer [17]) but is claimed to be able to represent linearly degenerate intermediate waves "with a minimum of smearing" by evaluating the eigenvalues and eigenvectors of the intermediate characteristic fields (given in Section 2.1).

There are iterative exact Riemann solvers for the equations of non-linear elasticity (to which the GPR model reduces as $\tau_1 \to \infty$). Thus, they will work for applications of the GPR model to solids problems (and perhaps to very viscous fluids problems too). Although these solvers are computationally expensive, they are only used once at each material interface point at each time step, and thus the added accuracy that they provide may be desirable. There are two ways to formulate the equations of non-linear elasticity: one in which the deformation tensor (the analogue of the inverse of the GPR model's distortion tensor) is evolved in time, and one in which its inverse (the analogue of A) is evolved instead. Miller's exact solver [27] uses the first formulation and the solver of Barton et al. [4] uses the second. The former can be used to evolve A^{-1}, from which A can be calculated. Unfortunately, both solvers critically assume that the source terms of the system vanish, and so are unlikely to produce the correct boundary conditions for the GPR-RGFM when modeling relatively inviscid fluids. It should also be noted that they cannot be used for problems involving heat conduction across material interfaces, and they do not take the thermal conduction subsystem of the GPR model into account.

If a different EOS is used in order to model solids or other kinds of fluids, the derivations of the primitive systems matrices of the GPR model (given in Section 6) will have to be performed again for each EOS, and the form of the eigenvectors will change (along with the systems solved to obtain the linearised approximations to the star states for use in the GPR-RGFM). Although this is tedious, it is a relatively straightforward derivation to perform.
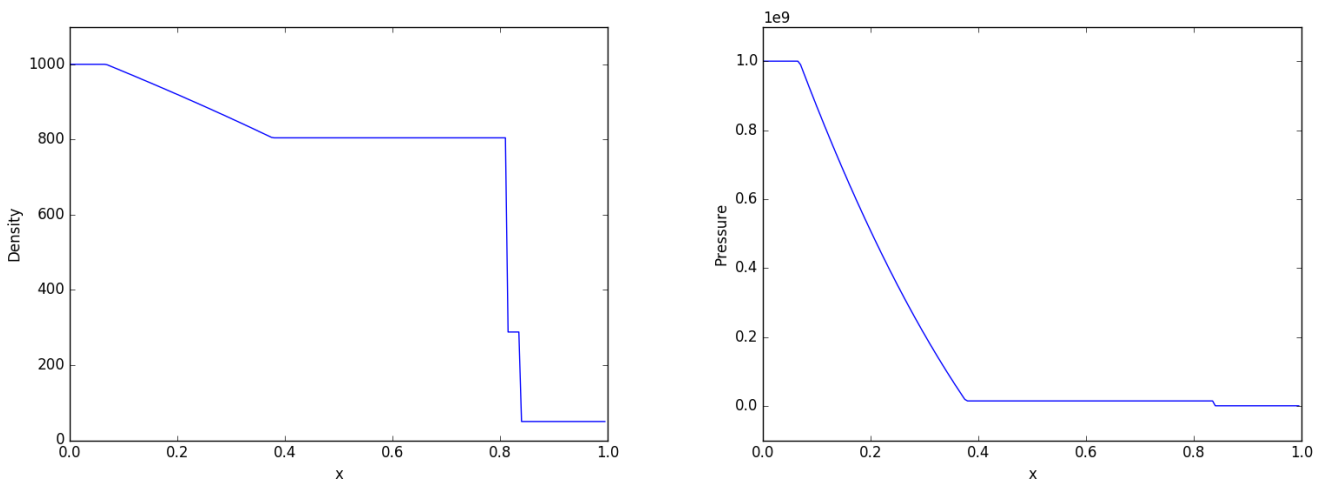
Figure 16: Density and pressure for the exact solution to the Euler equations for the water-gas shock tube test

5. References

[1] M. Aivazis, W. Goddard, D. Meiron, M. Ortiz, J. Pool, and J. Shepherd, *A virtual test facility for simulating the dynamic response of materials*, Computing in Science & Engineering, 2 (2000), pp. 39–50.

[2] F. Alcrudo and F. Benkhaldoun, *Exact solutions to the Riemann problem of the shallow water equations with a bottom step*, Computers & Fluids, 30 (2001), pp. 643–671.

[3] P. T. Barton and D. Drikakis, *An Eulerian method for multi-component problems in non-linear elasticity with sliding interfaces*, Journal of Computational Physics, 229 (2010), pp. 5518–5540.

[4] P. T. Barton, D. Drikakis, E. Romenski, and V. a. Titarev, *Exact and approximate solutions of Riemann problems in non-linear elasticity*, Journal of Computational Physics, 228 (2009), pp. 7046–7068.

[5] P. T. Barton, B. Obadia, and D. Drikakis, *A conservative level-set based method for compressible solid/fluid problems on fixed grids*, Journal of Computational Physics, 230 (2011), pp. 7867–7890.

[6] W. Boscheri, M. Dumbser, and R. Loubere, *Cell centered direct Arbitrary-Lagrangian-Eulerian ADER-WENO finite volume schemes for nonlinear hyperelasticity*, International Journal for Numerical Methods in Fluids, 135 (2016), pp. 111–129.

[7] A. Chinnayya, E. Daniel, and R. Saurel, *Modelling detonation waves in heterogeneous energetic materials*, Journal of Computational Physics, 196 (2004), pp. 490–538.

[8] M. Dumbser and D. S. Balsara, *A new efficient formulation of the HLLEM Riemann solver for general conservative and non-conservative hyperbolic systems*, Journal of Computational Physics, 304 (2016), pp. 275–319.

[9] M. Dumbser and D. S. Balsara, *A new efficient formulation of the HLLEM Riemann solver for general conservative and non-conservative hyperbolic systems*, Journal of Computational Physics, 304 (2016), pp. 275–319.

[10] M. Dumbser, I. Peshkov, E. Romenski, and O. Zanotti, *High order ADER schemes for a unified first order hyperbolic formulation of continuum mechanics: Viscous heat-conducting fluids and elastic solids*, Journal of Computational Physics, 314 (2016), pp. 824–862.

[11] R. Fedkiw, T. Aslam, B. Merriman, and S. Osher, *A Non-oscillatory Eulerian Approach to Interfaces in Multimaterial Flows (the Ghost Fluid Method)*, Journal of Computational Physics, 152 (1999), pp. 457–492.

[12] R. P. Fedkiw, *Coupling an Eulerian Fluid Calculation to a Lagrangian Solid Calculation with the Ghost Fluid Method*, Journal of Computational Physics, 175 (2002), pp. 200–224.

[13] J. Frenkel, *Kinetic Theory of Liquids*, Oxford University Press, 1947.

[14] N. S. Ghaisas, A. Subramaniam, and S. K. Lele, *High-Order Eulerian Methods for Elastic-Plastic Flow in Solids and Coupling with Fluid Flows*, 46th AIAA Fluid Dynamics Conference, (2016), pp. 1–17.

[15] J. Glimm and D. Marchesin, *A Numerical Method for Two Phase Flow with an Unstable Interface*, Journal of Computational Physics, 39 (1981), pp. 179–200.

[16] S. K. Godunov and E. I. Romenskii, *Nonstationary equations of nonlinear elasticity theory in eulerian coordinates*, Journal of Applied Mechanics & Technical Physics, 13 (1974), pp. 868–884.

[17] A. Harten, P. D. Lax, and B. van Leer, *On Upstream Differencing and Godunov-Type Schemes for Hyperbolic Conservation Laws*, SIAM Review, 25 (1983), pp. 35–61.

[18] C. W. Hirt and B. D. Nichols, *Volume of fluid (VOF) method for the dynamics of free boundaries*, Journal of Computational Physics, 39 (1981), pp. 201–225.

[19] G. Hou, J. Wang, and A. Layton, *Numerical methods for fluid-structure interaction - A review*, Communications in Computational Physics, 12 (2012), pp. 337–377.

[20] B. Hübner, E. Walhorn, and D. Dinkler, *A monolithic approach to fluid-structure interaction using space-time finite elements*, Computer Methods in Applied Mechanics & Engineering, 193 (2004), pp. 2087–2104.

[21] A. Legay, J. Chessa, and T. Belytschko, *An Eulerian-Lagrangian method for fluid-structure interaction based on level sets*, Computer Methods in Applied Mechanics & Engineering, 195 (2006), pp. 2070–2087.

[22] T. G. Liu, B. C. Khoo, and K. S. Yeo, *Ghost fluid method for strong shock impacting on material interface*, Journal of Computational Physics, 190 (2003), pp. 651–681.

[23] T.-P. Liu, *The Riemann problem for general systems of conservation laws*, Journal of Differential Equations, 18 (1975), pp. 218–234.

[24] A. N. Malyshev and E. I. Romenski, *Hyperbolic Equations for Heat Transfer. Global Solvability of the Cauchy Problem*, Sibirskii Matematicheskii Zhurnal, 27 (1984), pp. 128–134.

[25] L. Michael and N. Nikiforakis, *Coupling of elastoplastic solid models with condensed-phase explosives formulations*, (submitted), (2016).

[26] C. Michler, S. J. Hulshoff, E. H. van Brummelen, and R. de Borst, *A monolithic approach to fluid-structure interaction*, Computers & Fluids, 33 (2004), pp. 839–848.

[27] G. H. Miller, *An iterative Riemann solver for systems of hyperbolic conservation laws, with application to hyperelastic solid mechanics*, Journal of Computational Physics, 193 (2004), pp. 198–225.

[28] S. Osher and R. Fedkiw, *Level Set Methods and Dynamic Implicit Surfaces*, Springer, 2002.

[29] I. Peshkov and E. Romenski, *A hyperbolic model for viscous Newtonian flows*, Continuum Mechanics & Thermodynamics, 28 (2016), pp. 85–104.

[30] F. D. Pin, S. Idelsohn, E. Onate, and R. Aubry, *The ALE/Lagrangian Particle Finite Element Method: A new approach to computation of free-surface flows and fluid-object interactions*, Computers & Fluids, 36 (2007), pp. 27–38.

[31] E. Romenski, D. Drikakis, and E. Toro, *Conservative models and nu-*

merical methods for compressible two-phase flow*, Journal of Scientific Computing, 42 (2010), pp. 68–95.

[32] E. ROMENSKI, A. D. RESNYANSKY, AND E. F. TORO, *Conservative Hyperbolic Formulation for Compressible Two-Phase Flow with Different Phase Pressures and Temperatures*, Quarterly of Applied Mathematics, 65 (2007), pp. 259–279.

[33] E. I. ROMENSKI, *Hyperbolic Equations of Maxwell's Nonlinear Model of Elastoplastic Heat-Conducting Media*, Sibirskii Matematicheskii Zhurnal, 30 (1988), pp. 135–159.

[34] R. ROSSI AND E. OÑATE, *Analysis of some partitioned algorithms for fluid-structure interaction*, Engineering Computations, 27 (2010), pp. 20–56.

[35] P. B. RYZHAKOV, R. ROSSI, S. R. IDELSOHN, AND E. ONATE, *A monolithic Lagrangian approach for fluid-structure interaction problems*, Computational Mechanics, 46 (2010), pp. 883–899.

[36] S. K. SAMBASIVAN AND H. S. UDAYKUMAR, *Ghost Fluid Method for Strong Shock Interactions Part 1: Fluid-Fluid Interfaces*, AIAA Journal, 47 (2009), pp. 2907–2922.

[37] ———, *Ghost Fluid Method for Strong Shock Interactions Part 2: Immersed Solid Boundaries*, AIAA Journal, 47 (2009), pp. 2923–2937.

[38] S. SCHOCH, K. NORDIN-BATES, AND N. NIKIFORAKIS, *An Eulerian algorithm for coupled simulations of elastoplastic-solids and condensed-phase explosives*, Journal of Computational Physics, 252 (2013), pp. 163–194.

[39] E. F. TORO, *Riemann Solvers and Numerical Methods for Fluid Dynamics: A Practical Introduction*, Springer, 2009.

[40] S. P. WANG, M. H. ANDERSON, J. G. OAKLEY, M. L. CORRADINI, AND R. BONAZZA, *A thermodynamically consistent and fully conservative treatment of contact discontinuities for compressible multicomponent flows*, Journal of Computational Physics, 195 (2004), pp. 528–559.

6. Appendix

Taking the ordering $\boldsymbol{P}$ of primitive variables in (57), note that (1e), (1b), (1c), (1d) can be stated as:

$$\frac{D\rho}{Dt} + \rho \frac{\partial v_k}{\partial x_k} = 0 \tag{48a}$$

$$\frac{Dv_i}{Dt} + \frac{1}{\rho} \frac{\partial \Sigma_{ik}}{\partial x_k} = 0 \tag{48b}$$

$$\frac{DA_{ij}}{Dt} + A_{ik} \frac{\partial v_k}{\partial x_j} = -\frac{\psi_{ij}}{\theta_1} \tag{48c}$$

$$\frac{DJ_i}{Dt} + \frac{1}{\rho} \frac{\partial T\delta_{ik}}{\partial x_k} = -\frac{H_i}{\theta_2} \tag{48d}$$

$$\frac{DE}{Dt} + \frac{1}{\rho} \frac{\partial (\Sigma_{ik} v_i + TH_k)}{\partial x_k} = 0 \tag{48e}$$

where the stress tensor $\Sigma = pI + \rho A^T \psi$. Note that:

$$\frac{DE}{Dt} = \frac{\partial E}{\partial p}\frac{Dp}{Dt} + \frac{\partial E}{\partial \rho}\frac{D\rho}{Dt} + v_i \frac{Dv_i}{Dt} + \psi_{ij}\frac{DA_{ij}}{Dt} + H_i \frac{DJ_i}{Dt} \quad (49)$$

Thus, the energy equation becomes:

$$\frac{\partial E}{\partial p}\frac{Dp}{Dt} - \frac{\partial E}{\partial \rho}\rho \frac{\partial v_k}{\partial x_k} - \frac{v_i}{\rho}\frac{\partial \Sigma_{ik}}{\partial x_k} - \psi_{ij}A_{ik}\frac{\partial v_k}{\partial x_j} - \frac{\psi_{ij}\psi_{ij}}{\theta_1} \tag{50}$$
$$- \frac{H_i}{\rho}\frac{\partial T\delta_{ik}}{\partial x_k} - \frac{H_i H_i}{\theta_2} + \frac{1}{\rho}\frac{\partial(\Sigma_{ik}v_i + TH_k)}{\partial x_k} = 0$$

Simplifying:

$$\frac{\partial E}{\partial p}\frac{Dp}{Dt} + \left(\frac{p}{\rho} - \frac{\partial E}{\partial \rho}\rho\right)\frac{\partial v_k}{\partial x_k} + \frac{T}{\rho}\frac{\partial H_k}{\partial x_k} = \frac{\psi_{ij}\psi_{ij}}{\theta_1} + \frac{H_i H_i}{\theta_2} \tag{51}$$

The full system then becomes:

$$\frac{D\rho}{Dt} + \rho \frac{\partial v_k}{\partial x_k} = 0 \tag{52a}$$

$$\frac{Dv_i}{Dt} + \frac{1}{\rho}\frac{\partial \Sigma_{ik}}{\partial x_k} = 0 \tag{52b}$$

$$\frac{DA_{ij}}{Dt} + A_{ik}\frac{\partial v_k}{\partial x_j} = -\frac{\psi_{ij}}{\theta_1} \tag{52c}$$

$$\frac{DJ_i}{Dt} + \frac{1}{\rho}\frac{\partial T\delta_{ik}}{\partial x_k} = -\frac{H_i}{\theta_2} \tag{52d}$$

$$\frac{Dp}{Dt} + \frac{p - \rho^2 E_\rho}{\rho E_p}\frac{\partial v_k}{\partial x_k} + \frac{T}{\rho E_p}\frac{\partial H_k}{\partial x_k} = \frac{\psi_{ij}\psi_{ij}}{\theta_1 E_p} + \frac{H_i H_i}{\theta_2 E_p} \tag{52e}$$

Note that[4]:

$$\frac{p - \rho^2 E_\rho}{\rho E_p} = \rho c_0^2 \tag{54a}$$

$$\frac{\alpha^2 T}{\rho E_p} = \frac{\alpha^2 T}{\rho c_v T_p} = \frac{\rho c_h^2}{T_p} \tag{54b}$$

Thus, expressing the system in terms of spatial derivatives of the primitive variables, we have:

$$\frac{D\rho}{Dt} + \rho \frac{\partial v_k}{\partial x_k} = 0 \tag{55a}$$

$$\frac{Dv_i}{Dt} + \frac{\delta_{ik}}{\rho}\frac{\partial p}{\partial x_k} - \frac{\sigma_{ik}}{\rho^2}\frac{\partial \rho}{\partial x_k} - \frac{1}{\rho}\frac{\partial \sigma_{ik}}{\partial A_{mn}}\frac{\partial A_{mn}}{\partial x_k} = 0 \tag{55b}$$

$$\frac{DA_{ij}}{Dt} + A_{ik}\frac{\partial v_k}{\partial x_j} = -\frac{\psi_{ij}}{\theta_1} \tag{55c}$$

$$\frac{DJ_i}{Dt} + \frac{T_\rho \delta_{ik}}{\rho}\frac{\partial \rho}{\partial x_k} + \frac{T_p \delta_{ik}}{\rho}\frac{\partial p}{\partial x_k} = -\frac{H_i}{\theta_2} \tag{55d}$$

$$\frac{Dp}{Dt} + \rho c_0^2 \frac{\partial v_k}{\partial x_k} + \frac{\rho c_h^2}{T_p}\frac{\partial J_k}{\partial x_k} = \frac{\|\psi\|_F^2}{\theta_1 E_p} + \frac{\|H\|^2}{\theta_2 E_p} \tag{55e}$$

Thus, the GPR system can be written in the following form:

$$\frac{\partial \boldsymbol{P}}{\partial t} + \boldsymbol{M} \cdot \nabla \boldsymbol{P} = \boldsymbol{S_p} \tag{56}$$

---

[4]

$$\frac{p - \rho^2 E_\rho}{\rho E_p} = \frac{\rho^2 \left.E_\rho\right|_s - \rho^2 \left.E_\rho\right|_p}{\rho \left.E_p\right|_\rho} = \rho \frac{\left.E_\rho\right|_s - \left(\left.E_\rho\right|_s + E_s|_\rho \left.s_\rho\right|_p\right)}{E_s|_\rho \left.s_p\right|_\rho} \tag{53}$$

$$= \rho \frac{-\left.s_\rho\right|_p}{\left.s_p\right|_\rho} = \rho \left.\frac{\partial p}{\partial \rho}\right|_s$$

The result follows by the definition of c_0.

$$M_1 =
\begin{pmatrix}
v_1 & 0 & 0 & 0 & 0 & 0 & 0 & 0 & 0 & 0 & 0 & -\frac{\sigma_{11}}{\rho^2} & -\frac{\sigma_{21}}{\rho^2} & -\frac{\sigma_{31}}{\rho^2} & \frac{T_p}{\rho} & 0 & 0 \\[4pt]
0 & v_1 & 0 & 0 & 0 & 0 & 0 & 0 & 0 & 0 & 0 & \frac{1}{\rho} & 0 & 0 & \frac{T_p}{\rho} & 0 & 0 \\[4pt]
0 & 0 & v_1 & 0 & 0 & 0 & 0 & 0 & 0 & 0 & 0 & -\frac{1}{\rho}\frac{\partial\sigma_{11}}{\partial A_{11}} & -\frac{1}{\rho}\frac{\partial\sigma_{21}}{\partial A_{11}} & -\frac{1}{\rho}\frac{\partial\sigma_{31}}{\partial A_{11}} & 0 & 0 & 0 \\[4pt]
0 & 0 & 0 & v_1 & 0 & 0 & 0 & 0 & 0 & 0 & 0 & -\frac{1}{\rho}\frac{\partial\sigma_{11}}{\partial A_{21}} & -\frac{1}{\rho}\frac{\partial\sigma_{21}}{\partial A_{21}} & -\frac{1}{\rho}\frac{\partial\sigma_{31}}{\partial A_{21}} & 0 & 0 & 0 \\[4pt]
0 & 0 & 0 & 0 & v_1 & 0 & 0 & 0 & 0 & 0 & 0 & -\frac{1}{\rho}\frac{\partial\sigma_{11}}{\partial A_{31}} & -\frac{1}{\rho}\frac{\partial\sigma_{21}}{\partial A_{31}} & -\frac{1}{\rho}\frac{\partial\sigma_{31}}{\partial A_{31}} & 0 & 0 & 0 \\[4pt]
0 & 0 & 0 & 0 & 0 & v_1 & 0 & 0 & 0 & 0 & 0 & -\frac{1}{\rho}\frac{\partial\sigma_{11}}{\partial A_{12}} & -\frac{1}{\rho}\frac{\partial\sigma_{21}}{\partial A_{12}} & -\frac{1}{\rho}\frac{\partial\sigma_{31}}{\partial A_{12}} & 0 & 0 & 0 \\[4pt]
0 & 0 & 0 & 0 & 0 & 0 & v_1 & 0 & 0 & 0 & 0 & -\frac{1}{\rho}\frac{\partial\sigma_{11}}{\partial A_{22}} & -\frac{1}{\rho}\frac{\partial\sigma_{21}}{\partial A_{22}} & -\frac{1}{\rho}\frac{\partial\sigma_{31}}{\partial A_{22}} & 0 & 0 & 0 \\[4pt]
0 & 0 & 0 & 0 & 0 & 0 & 0 & v_1 & 0 & 0 & 0 & -\frac{1}{\rho}\frac{\partial\sigma_{11}}{\partial A_{32}} & -\frac{1}{\rho}\frac{\partial\sigma_{21}}{\partial A_{32}} & -\frac{1}{\rho}\frac{\partial\sigma_{31}}{\partial A_{32}} & 0 & 0 & 0 \\[4pt]
0 & 0 & 0 & 0 & 0 & 0 & 0 & 0 & v_1 & 0 & 0 & -\frac{1}{\rho}\frac{\partial\sigma_{11}}{\partial A_{13}} & -\frac{1}{\rho}\frac{\partial\sigma_{21}}{\partial A_{13}} & -\frac{1}{\rho}\frac{\partial\sigma_{31}}{\partial A_{13}} & 0 & 0 & 0 \\[4pt]
0 & 0 & 0 & 0 & 0 & 0 & 0 & 0 & 0 & v_1 & 0 & -\frac{1}{\rho}\frac{\partial\sigma_{11}}{\partial A_{23}} & -\frac{1}{\rho}\frac{\partial\sigma_{21}}{\partial A_{23}} & -\frac{1}{\rho}\frac{\partial\sigma_{31}}{\partial A_{23}} & 0 & 0 & 0 \\[4pt]
0 & 0 & 0 & 0 & 0 & 0 & 0 & 0 & 0 & 0 & v_1 & -\frac{1}{\rho}\frac{\partial\sigma_{11}}{\partial A_{33}} & -\frac{1}{\rho}\frac{\partial\sigma_{21}}{\partial A_{33}} & -\frac{1}{\rho}\frac{\partial\sigma_{31}}{\partial A_{33}} & 0 & 0 & 0 \\[4pt]
\rho & \rho c_0^2 & A_{11} & A_{21} & A_{31} & 0 & 0 & 0 & 0 & 0 & 0 & v_1 & 0 & 0 & 0 & 0 & 0 \\[4pt]
0 & 0 & A_{12} & A_{22} & A_{32} & 0 & 0 & 0 & 0 & 0 & 0 & 0 & v_1 & 0 & 0 & 0 & 0 \\[4pt]
0 & 0 & A_{13} & A_{23} & A_{33} & 0 & 0 & 0 & 0 & 0 & 0 & 0 & 0 & v_1 & 0 & 0 & 0 \\[4pt]
0 & \frac{\rho c_h^2}{T_p} & 0 & 0 & 0 & 0 & 0 & 0 & 0 & 0 & 0 & 0 & 0 & 0 & v_1 & 0 & 0 \\[4pt]
0 & 0 & 0 & 0 & 0 & 0 & 0 & 0 & 0 & 0 & 0 & 0 & 0 & 0 & 0 & v_1 & 0 \\[4pt]
0 & 0 & 0 & 0 & 0 & 0 & 0 & 0 & 0 & 0 & 0 & 0 & 0 & 0 & 0 & 0 & v_1
\end{pmatrix}$$

$$
M_2 =
\begin{pmatrix}
\nu_2 & 0 & \rho & 0 & 0 & 0 & 0 & 0 & 0 & 0 & 0 & 0 & 0 & 0 & 0 & 0 & 0 \\[4pt]
-\dfrac{\sigma_{12}}{\rho^2} & \nu_2 & 0 & 0 & -\dfrac{1}{\rho}\dfrac{\partial\sigma_{12}}{\partial A_{11}} & -\dfrac{1}{\rho}\dfrac{\partial\sigma_{12}}{\partial A_{21}} & -\dfrac{1}{\rho}\dfrac{\partial\sigma_{12}}{\partial A_{31}} & -\dfrac{1}{\rho}\dfrac{\partial\sigma_{12}}{\partial A_{12}} & -\dfrac{1}{\rho}\dfrac{\partial\sigma_{12}}{\partial A_{22}} & -\dfrac{1}{\rho}\dfrac{\partial\sigma_{12}}{\partial A_{32}} & -\dfrac{1}{\rho}\dfrac{\partial\sigma_{12}}{\partial A_{13}} & -\dfrac{1}{\rho}\dfrac{\partial\sigma_{12}}{\partial A_{23}} & -\dfrac{1}{\rho}\dfrac{\partial\sigma_{12}}{\partial A_{33}} & 0 & 0 & 0 & \dfrac{T_p}{\rho} \\[4pt]
-\dfrac{\sigma_{22}}{\rho^2} & 0 & \nu_2 & 0 & -\dfrac{1}{\rho}\dfrac{\partial\sigma_{22}}{\partial A_{11}} & -\dfrac{1}{\rho}\dfrac{\partial\sigma_{22}}{\partial A_{21}} & -\dfrac{1}{\rho}\dfrac{\partial\sigma_{22}}{\partial A_{31}} & -\dfrac{1}{\rho}\dfrac{\partial\sigma_{22}}{\partial A_{12}} & -\dfrac{1}{\rho}\dfrac{\partial\sigma_{22}}{\partial A_{22}} & -\dfrac{1}{\rho}\dfrac{\partial\sigma_{22}}{\partial A_{32}} & -\dfrac{1}{\rho}\dfrac{\partial\sigma_{22}}{\partial A_{13}} & -\dfrac{1}{\rho}\dfrac{\partial\sigma_{22}}{\partial A_{23}} & -\dfrac{1}{\rho}\dfrac{\partial\sigma_{22}}{\partial A_{33}} & 0 & 0 & \dfrac{1}{\rho} & \dfrac{T_p}{\rho} \\[4pt]
-\dfrac{\sigma_{32}}{\rho^2} & 0 & 0 & \nu_2 & -\dfrac{1}{\rho}\dfrac{\partial\sigma_{32}}{\partial A_{11}} & -\dfrac{1}{\rho}\dfrac{\partial\sigma_{32}}{\partial A_{21}} & -\dfrac{1}{\rho}\dfrac{\partial\sigma_{32}}{\partial A_{31}} & -\dfrac{1}{\rho}\dfrac{\partial\sigma_{32}}{\partial A_{12}} & -\dfrac{1}{\rho}\dfrac{\partial\sigma_{32}}{\partial A_{22}} & -\dfrac{1}{\rho}\dfrac{\partial\sigma_{32}}{\partial A_{32}} & -\dfrac{1}{\rho}\dfrac{\partial\sigma_{32}}{\partial A_{13}} & -\dfrac{1}{\rho}\dfrac{\partial\sigma_{32}}{\partial A_{23}} & -\dfrac{1}{\rho}\dfrac{\partial\sigma_{32}}{\partial A_{33}} & 0 & 0 & 0 & 0 \\[4pt]
0 & 0 & \nu_2 & 0 & \nu_2 & 0 & 0 & 0 & 0 & 0 & 0 & 0 & 0 & 0 & 0 & 0 & 0 \\[2pt]
0 & 0 & 0 & \nu_2 & 0 & \nu_2 & 0 & 0 & 0 & 0 & 0 & 0 & 0 & 0 & 0 & 0 & 0 \\[2pt]
0 & 0 & 0 & 0 & 0 & 0 & \nu_2 & 0 & 0 & 0 & 0 & 0 & 0 & 0 & 0 & 0 & 0 \\[2pt]
0 & 0 & 0 & 0 & 0 & 0 & 0 & \nu_2 & 0 & 0 & 0 & 0 & 0 & 0 & 0 & 0 & 0 \\[2pt]
0 & 0 & 0 & 0 & 0 & 0 & 0 & 0 & \nu_2 & 0 & 0 & 0 & 0 & 0 & 0 & 0 & 0 \\[2pt]
0 & 0 & \nu_2 & 0 & 0 & 0 & 0 & 0 & 0 & \nu_2 & 0 & 0 & 0 & 0 & 0 & 0 & 0 \\[2pt]
0 & 0 & 0 & 0 & 0 & 0 & 0 & 0 & 0 & 0 & \nu_2 & 0 & 0 & 0 & 0 & 0 & 0 \\[2pt]
\rho & A_{11} & A_{21} & A_{31} & 0 & 0 & 0 & 0 & 0 & 0 & 0 & \nu_2 & 0 & 0 & 0 & 0 & 0 \\[2pt]
\rho c_0^2 & A_{12} & A_{22} & A_{32} & 0 & 0 & 0 & 0 & 0 & \nu_2 & 0 & 0 & 0 & 0 & 0 & 0 & 0 \\[2pt]
0 & A_{13} & A_{23} & A_{33} & 0 & 0 & 0 & 0 & \nu_2 & 0 & 0 & 0 & 0 & 0 & 0 & 0 & 0 \\[2pt]
0 & 0 & 0 & 0 & 0 & 0 & 0 & \nu_2 & 0 & 0 & 0 & 0 & 0 & 0 & 0 & 0 & 0 \\[2pt]
\dfrac{\rho c_h^2}{T_p} & 0 & 0 & 0 & 0 & 0 & 0 & 0 & 0 & 0 & 0 & 0 & 0 & \nu_2 & 0 & 0 & 0 \\[2pt]
0 & 0 & 0 & 0 & 0 & 0 & 0 & 0 & 0 & 0 & 0 & 0 & 0 & 0 & \nu_2 & 0 & 0
\end{pmatrix}
$$

$$
M_3 =
\begin{pmatrix}
0 & \frac{\rho c_h^2}{T_p} & 0 & 0 & 0 & 0 & 0 & 0 & 0 & 0 & 0 & 0 & 0 & 0 & 0 & 0 & v_3 \\[4pt]
0 & 0 & 0 & 0 & 0 & 0 & 0 & 0 & 0 & 0 & 0 & 0 & 0 & 0 & 0 & v_3 & 0 \\[4pt]
0 & 0 & 0 & 0 & 0 & 0 & 0 & 0 & 0 & 0 & 0 & 0 & 0 & 0 & v_3 & 0 & 0 \\[4pt]
\rho & \rho c_0^2 & 0 & 0 & 0 & 0 & 0 & 0 & A_{13} & A_{23} & A_{33} & 0 & 0 & v_3 & 0 & 0 & 0 \\[4pt]
0 & 0 & 0 & 0 & 0 & 0 & 0 & 0 & A_{12} & A_{22} & A_{32} & 0 & v_3 & 0 & 0 & 0 & 0 \\[4pt]
0 & 0 & 0 & 0 & 0 & 0 & 0 & 0 & A_{11} & A_{21} & A_{31} & v_3 & 0 & 0 & 0 & 0 & 0 \\[4pt]
0 & 0 & 0 & 0 & 0 & 0 & 0 & 0 & 0 & 0 & v_3 & -\frac{1}{\rho}\frac{\partial\sigma_{13}}{\partial A_{33}} & -\frac{1}{\rho}\frac{\partial\sigma_{23}}{\partial A_{33}} & -\frac{1}{\rho}\frac{\partial\sigma_{33}}{\partial A_{33}} & 0 & 0 & 0 \\[4pt]
0 & 0 & 0 & 0 & 0 & 0 & 0 & 0 & 0 & v_3 & 0 & -\frac{1}{\rho}\frac{\partial\sigma_{13}}{\partial A_{23}} & -\frac{1}{\rho}\frac{\partial\sigma_{23}}{\partial A_{23}} & -\frac{1}{\rho}\frac{\partial\sigma_{33}}{\partial A_{23}} & 0 & 0 & 0 \\[4pt]
0 & 0 & 0 & 0 & 0 & 0 & 0 & 0 & v_3 & 0 & 0 & -\frac{1}{\rho}\frac{\partial\sigma_{13}}{\partial A_{13}} & -\frac{1}{\rho}\frac{\partial\sigma_{23}}{\partial A_{13}} & -\frac{1}{\rho}\frac{\partial\sigma_{33}}{\partial A_{13}} & 0 & 0 & 0 \\[4pt]
0 & 0 & 0 & 0 & 0 & 0 & 0 & v_3 & 0 & 0 & 0 & -\frac{1}{\rho}\frac{\partial\sigma_{13}}{\partial A_{32}} & -\frac{1}{\rho}\frac{\partial\sigma_{23}}{\partial A_{32}} & -\frac{1}{\rho}\frac{\partial\sigma_{33}}{\partial A_{32}} & 0 & 0 & 0 \\[4pt]
0 & 0 & 0 & 0 & 0 & 0 & v_3 & 0 & 0 & 0 & 0 & -\frac{1}{\rho}\frac{\partial\sigma_{13}}{\partial A_{22}} & -\frac{1}{\rho}\frac{\partial\sigma_{23}}{\partial A_{22}} & -\frac{1}{\rho}\frac{\partial\sigma_{33}}{\partial A_{22}} & 0 & 0 & 0 \\[4pt]
0 & 0 & 0 & 0 & 0 & v_3 & 0 & 0 & 0 & 0 & 0 & -\frac{1}{\rho}\frac{\partial\sigma_{13}}{\partial A_{12}} & -\frac{1}{\rho}\frac{\partial\sigma_{23}}{\partial A_{12}} & -\frac{1}{\rho}\frac{\partial\sigma_{33}}{\partial A_{12}} & 0 & 0 & 0 \\[4pt]
0 & 0 & 0 & 0 & v_3 & 0 & 0 & 0 & 0 & 0 & 0 & -\frac{1}{\rho}\frac{\partial\sigma_{13}}{\partial A_{31}} & -\frac{1}{\rho}\frac{\partial\sigma_{23}}{\partial A_{31}} & -\frac{1}{\rho}\frac{\partial\sigma_{33}}{\partial A_{31}} & 0 & 0 & 0 \\[4pt]
0 & 0 & 0 & v_3 & 0 & 0 & 0 & 0 & 0 & 0 & 0 & -\frac{1}{\rho}\frac{\partial\sigma_{13}}{\partial A_{21}} & -\frac{1}{\rho}\frac{\partial\sigma_{23}}{\partial A_{21}} & -\frac{1}{\rho}\frac{\partial\sigma_{33}}{\partial A_{21}} & 0 & 0 & 0 \\[4pt]
0 & 0 & v_3 & 0 & 0 & 0 & 0 & 0 & 0 & 0 & 0 & -\frac{1}{\rho}\frac{\partial\sigma_{13}}{\partial A_{11}} & -\frac{1}{\rho}\frac{\partial\sigma_{23}}{\partial A_{11}} & -\frac{1}{\rho}\frac{\partial\sigma_{33}}{\partial A_{11}} & 0 & 0 & 0 \\[4pt]
0 & v_3 & 0 & 0 & 0 & 0 & 0 & 0 & 0 & 0 & 0 & 0 & 0 & -\frac{1}{\rho} & 0 & 0 & \frac{T_p}{\rho} \\[4pt]
v_3 & 0 & 0 & 0 & 0 & 0 & 0 & 0 & 0 & 0 & 0 & -\frac{\sigma_{13}}{\rho^2} & -\frac{\sigma_{23}}{\rho^2} & -\frac{\sigma_{33}}{\rho^2} & 0 & 0 & \frac{T_p}{\rho}
\end{pmatrix}
$$

$$\boldsymbol{P} = \begin{pmatrix} \rho \\ p \\ A_{11} \\ A_{21} \\ A_{31} \\ A_{12} \\ A_{22} \\ A_{32} \\ A_{13} \\ A_{23} \\ A_{33} \\ v_1 \\ v_2 \\ v_3 \\ J_1 \\ J_2 \\ J_3 \end{pmatrix} \tag{57}$$

$$\boldsymbol{S_p} = \frac{1}{\theta_1\left(\tau_1\right) E_p} \begin{pmatrix} 0 \\ \|\psi\|_F^2 \\ 0 \\ 0 \\ 0 \\ -\psi_{11} \\ -\psi_{21} \\ -\psi_{31} \\ -\psi_{12} \\ -\psi_{22} \\ -\psi_{32} \\ -\psi_{13} \\ -\psi_{23} \\ -\psi_{33} \\ 0 \\ 0 \\ 0 \end{pmatrix} + \frac{1}{\theta_2\left(\tau_2\right) E_p} \begin{pmatrix} 0 \\ \|\boldsymbol{H}\|^2 \\ 0 \\ 0 \\ 0 \\ 0 \\ 0 \\ 0 \\ 0 \\ 0 \\ 0 \\ 0 \\ 0 \\ 0 \\ -H_1 \\ -H_2 \\ -H_3 \end{pmatrix} \tag{58}$$